29

Video-Rate Confocal Microscopy

Roger Y. Tsien and Brian J. Bacskai

WHY TRY TO REACH VIDEO-RATE?

Most current confocal laser-scanning microscopes require >0.1 sec, more typically ~1 sec, to complete a single full scan of the field of view. Such speeds are considerably slower than conventional video displays or the psychophysical flicker-fusion frequency, so they give the visual impression of discontinuous image acquisition, rather than a smoothly evolving scene. This speed limitation is imposed by the scanning rates of conventional scanners based on linear servo galvanometers, not from any inherent feature of the confocal principle. Scanning at video rate has many advantages. The most obvious but not necessarily the most important is the psychophysical appearance of smooth motion or evolution, which greatly aids the user to locate and focus on regions of interest. Many biochemical signals inside living cells, particularly membrane potential and cytosolic free Ca^{2+} and Na^{+}, undergo changes in the time scale of seconds down to tenths of milliseconds. Such signals are especially important in neurobiology because neurons rely on such biochemistry to perform their special function of fast information processing. The ability of confocal microscopy to generate optical sections without physically slicing or damaging the specimen is most valuable in complex three-dimensional living tissues, whereas in dead fixed material, the superiority of confocal microscopy over physical serial sectioning is a matter of convenience rather than principle. Even when relatively slow events occurring on the time scale of seconds to tens of seconds are being observed, high-speed imaging is important if one wishes to monitor these changes throughout a significant volume requiring many distinct planes of focus. A final, and perhaps subtle, advantage of high-speed scanning is that triplet-state saturation of the fluorophores should be considerably lessened by reducing the dwell-time/pixel to about 0.1 μsec instead of the >1 μsec typical of slow scanning (see Chapter 16, *this volume*).

Current attempts to reach higher scan rates have aimed at video-rate scanning, defined here as imaging 25 or 30 complete rasters/sec (corresponding to European vs. U.S./Japanese broadcast standards), each raster consisting of >480 scan lines. Adherence to broadcast standard rates has the tremendous advantage of compatibility with readily available video equipment such as image processors, monitors, videotape and laser disk recorders. Even higher frame rates are conceivable but will encounter a tremendous jump in cost unless the number of scan lines is reduced in proportion, so as to keep the overall pixel rate and signal bandwidth constant.

In the absence of true video-scanning, many workers observing rapid physiological signals have obtained time-resolution from slow-scanning confocal microscopes by "line-scanning." The vertical scan is disabled, so that successive views of the same physical line are acquired every 1–2 msec and displayed progressively from the top of the screen to the bottom in an x vs. t format. This display scheme can be a useful compromise when one knows or can guess where to fix the physical line to be repetitively scanned. However, when dynamics can occur anywhere within the field of view, line scanning is frustrating because it reduces the field of view to the width of just one line.

ADVANTAGES AND DISADVANTAGES OF NIPKOW DISKS, SLIT SCANS, AND POINT LASER SCANS

Nipkow disks and slit-scanning systems are more thoroughly covered in Chapters 10 and 25. Nipkow disk systems typically use a wide-field nonlaser, source such as an arc lamp, which illuminates an opaque mask with a spiral pattern of pinholes or slits inserted in a plane optically conjugate with the specimen. Rotation of the disk scans the apertures across the specimen. Reflected light or fluorescence emission is filtered by the very same apertures; the final image is detected by the naked eye, photographic film, or a conventional or slow-scan video camera whose internal raster scan is not synchronized to the illumination scanning. The average incident light intensity is greatly reduced compared to a conventional wide-field microscope system because the mask transmits only 1–2% of the excitation light. This loss is affordable in reflected light imaging because the light that returns from the specimen is relatively abundant and is unchanged in wavelength. However, typical biological specimens with weak fluorescence staining become so dim as to require fairly long camera integration periods, either on the CCD chip itself or by digital averaging in an image processor. Such integration effectively negates the speed advantage obtained by having multiple apertures. Furthermore, the use of the very same physical apertures for both excitation and emission places stringent limits on chromatic aberration (CA), which probably rules out ultraviolet (UV) excitation with existing refractive objectives. By contrast, physical separation of the excitation and

Roger Y. Tsien and Brian J. Bacskai • Howard Hughes Medical Institute and Department of Pharmacology 0647, University of California, San Diego, 9500 Gilman Drive, La Jolla, California 92093-0647.

Handbook of Biological Confocal Microscopy, edited by James B. Pawley. Plenum Press, New York, 1995.

emission apertures in a CLSM permits their diameters and their focus positions to be separately optimized. By moving one or another pinhole along the optical axis, one can compensate for longitudinal CA.

Slit scanners have their own problems such as asymmetrical *x-y* resolution and reduced rejection of out-of-focus fluorescence (Gan and Sheppard, 1993; see also Chapters 3 and 25, *this volume*). In addition, point scanning and nonimaging detection still have fundamental advantages over line scanning and camera detection. Nonimaging detectors such as photomultiplier tubes (PMTs) and photodiodes are simpler and have higher quantum efficiency than their imaging counterparts such as microchannel-plate-intensified video cameras or CCDs, because reading a huge array of detectors is fundamentally more difficult than reading just one detector. With nonimaging detectors, it is relatively trivial to ratio two emission channels as required for many quantitative biochemical studies, since the emission beam can simply be split with a dichroic mirror after it has already been descanned and when it no longer has any spatial complexity. By contrast, ratioing of two emission channels with cameras either requires sequential observation of the two wavelengths, which is slow and wastes photons, or the purchase of two expensive cameras and careful registration of all their corresponding pixels (see Chapters 10 and 16, *this volume*). Finally, the promising new technique of two-photon excitation (Denk *et al.*, 1990) requires extremely high local photon fluxes that can only be achieved when a pulsed laser is focused to a near-diffraction-limited spot. Therefore, point scanning is essential to take advantage of the two-photon method.

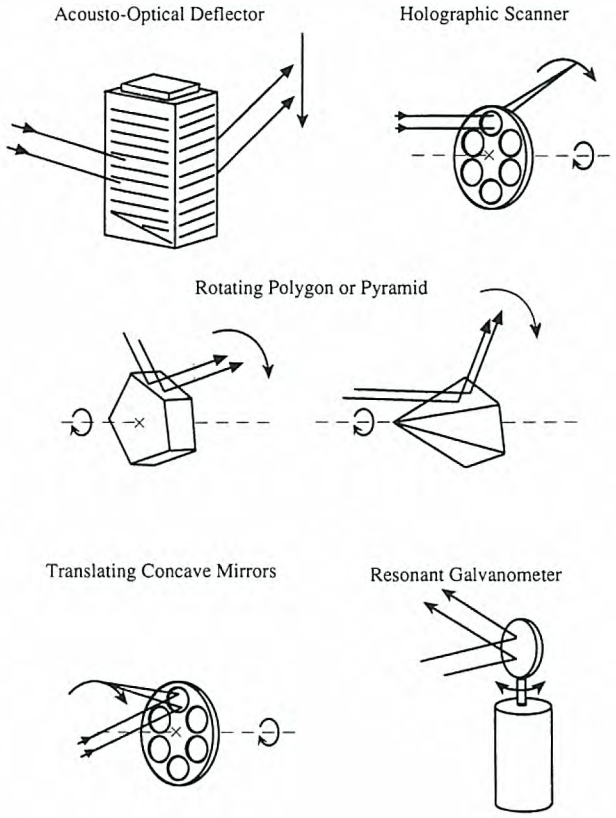

FIGURE 1. Schematic means for video-rate scanning. In acousto-optical deflection, sound waves (depicted as multiple parallel planes) are generated by a transducer at one end of a crystal and are absorbed by a nonreflecting wedge at the other end. Collimated light is diffracted by the pressure-induced changes in refractive index. The deflection angle is controllable by the λ and frequency of the sound waves, so that the output beam can be scanned in the direction parallel to the long axis of the crystal. In a holographic scanner, multiple holograms are recorded on a clear disk; each hologram deflects and focuses the incoming collimated beam. As the disk spins, the focus describes an arc around the rotation axis, flying back to its starting point as one hologram replaces another in the beam path. In rotating polygons and pyramids, the beam bounces off mirrored facets; the scan angle is $720°/m$ or $360°/m$, respectively, where m is the number of facets. Translating concave mirrors are carved by micromachining into a reflective substrate. They focus and scan the incoming beam analogously to a holographic scanner but are achromatic. A resonant galvanometer is a small flat mirror executing sinusoidal angular motion at the mechanically resonant frequency of its suspension.

HORIZONTAL SCANNING AT > 15 KHz

Video-rate point-scanning requires a horizontal scan frequency of 30 × 525 = 15,750 Hz for U.S./Japanese or 25 × 625 = 15,625 Hz for European standards. These rates are far too fast for linear servo galvanometers, which are currently limited to scan rates in the low-kHz range. At least four techniques, schematically depicted in Fig. 1, can scan at the requisite rates: (1) diffraction-grating-based methods, such as acousto-optical deflection or rotating holographic gratings; (2) rotating polygon mirrors; (3) multiple translating concave mirrors; and (4) resonant galvanometer mirrors. Advantages and disadvantages of each technique (R. Webb, 1984; Marshall, 1991; Art and Goodman, 1993) will be discussed in turn.

Diffraction-Grating-Based Methods

Acousto-Optical Deflection (AOD)

Acousto-optical deflection (Fig. 1; Gottlieb, 1991) uses ultrasonic waves to generate standing or traveling waves in a crystal. These pressure waves form an optical phase grating, which can diffract incident light and deflect it. Varying the input sound frequency varies the grating pitch and hence the deflection angle. The great advantage of acousto-optical deflection is that it has no mechanically moving parts and negligible inertia, so that it can produce sawtooth rasters with great accuracy and almost instantaneous flyback. Also, it can produce arbitrary deflections and, therefore, is the only scanner that can perform random-addressing. Unfortunately, acousto-optical deflection has significant disadvantages. As noted above, it is inherently dispersive (i.e., different λs are deflected differently), so that it is suited only to monochromatic laser excitation and transmitted or reflected light of the same λ (Webb, 1984). Only one single line of a laser can be used at a time; a change of excitation λs will cause an image shift that requires compensation. Fluorescence emissions occupy a broad band of λs longer than the excitation, so they cannot be descanned by the acousto-optical scanner. One innovative but difficult solution to this problem (Goldstein *et al.*, 1990, 1992) is not to send the emission back through any scanner but rather to detect it with an image dissector tube. This device is somewhat like a cathode ray tube in reverse in that at any given moment, only one spot on the face plate is photosensitive, and the location of the spot can be

selected by electrostatic or magnetic deflection. If the sensitive location can be electronically scanned in perfect registration with the excitation raster, confocal detection results. Unfortunately, because the acousto-optical deflector and image dissector are completely separate devices, maintaining perfect registration during rapid scanning is a major challenge. A more popular solution has been to use an acousto-optical deflector for the fast horizontal scan and a conventional servo galvanometer for the slow vertical scan. The emission is descanned only along the latter dimension and collected through a slit rather than a pinhole (Draaijer and Houpt, 1988, 1993), thus partially sacrificing confocality (Gan and Sheppard, 1993). There are a number of choices for the acousto-optical medium. Tellurium dioxide is a particularly efficient material for visible λs (Gottlieb, 1991) but is rather expensive and transmits UV poorly. For deep UV (200–360 nm), quartz must be used. Ordinary glass (BK7) is a cheap material usable in the same spectral regions as normal microscope optics. A further disadvantage of the AOD is that cylindrical lens elements are required to match the laser beam with the rectangular aperture of the crystal. The AOD itself contributes cylindrical lens power during fast scans, because the acoustic frequency and deflection angle then vary across the face of the AOD. Maintaining diffraction-limited wavefront quality is a nontrivial problem that can be solved by careful design. Femtosecond pulses as required for two-photon excitation may suffer significant group-velocity dispersion upon transit through the thick crystal. Such pulses also must inherently include a range of λs, which will be unequally deflected by the acoustic diffraction grating. Despite these problems, commercial systems have been successfully developed not only for reflectance imaging of semi-conductor wafers (Lasertec Corp., Yokohama, Japan; see Appendix I, *this volume*) but also for fluorescence imaging of biological specimens (Odyssey, Noran Instruments, Middleton, WI). The Noran instrument, which has been discussed before (Art and Goodman, 1993; Draaijer and Houpt, 1993), will be described in greater detail toward the end of this chapter.

Rotating Holographic Grating

Holographic scanners (Fig. 1; Dickson and Sincerbox, 1991; Kramer, 1991) are flat disks onto which a holographic grating has been impressed such that an incident beam arriving normal to the plane of the disk is deflected at an oblique angle. Rotation of the disk makes the reflected beam sweep out segments of a cone, which can be transformed by relay optics into a raster scan. Because holographic scanners are dispersive, yet require high-speed rotation, they do not appear to have any advantages for confocal microscopy.

Rotating Polygon Mirrors

Rotating polygons with mirror surfaces (Fig. 1) (Sherman, 1991) are the oldest technology for rapidly deflecting a light beam, whose application dates back to early measurements of the velocity of light by Foucault and Michelson during the 1860s and 1920s (Froome and Essen, 1969). The prototype confocal microscope built at the Medical Research Council, Cambridge, England, used a polygon scanner (White *et al.,* 1987), subsequently replaced by a linear servo galvanometer in the production model marketed by BioRad (Hemel, Hempstead, UK). Rotating polygons are optically simple, nondispersive, and naturally cause the output beam to follow a simple sawtooth raster that nicely mimics conventional video scanning. Unfortunately, rotating polygons have numerous drawbacks. Each facet of the polygon is ever so slightly different in reflectivity and angle with respect to axis of rotation. Those angular differences, known as pyramidal errors, combine with any wobble in the bearings to cause the beam to fluctuate in the (vertical) direction orthogonal to the (horizontal) scan direction unless additional optical corrections are applied. If the number of facets of the polygon is not an integral division of the total number of raster lines (525 or 625), this vertical wobble causes vernier ripple to propagate down the resulting images. The human visual system is exquisitely sensitive to such traveling vernier displacements, so the overall visual effect has been picturesquely described as similar to viewing a scene through a window down which rain is pouring (Webb *et al.,* 1987). If, however, the number of facets is an integral divisor of the number of raster lines, the vernier errors are stationary, eliminating the rainy window appearance. Unfortunately, polygons of 15, 25, or 75 sides are nonstandard. Moreover the peak-to-peak optical scan angle of a rotating polygon is fixed at $720°/m$ where m is the number of facets. For $m = 15$, 25 or 75, the scan angles are 48°, 28.8°, or 9.6°, respectively, significantly larger than the acceptance angles of microscope objectives, typically around 7°. Therefore, demagnifying relay optics will be required. Polygons of 15, 25, or 75 sides must rotate at 63, 37.8 or 12.6×10^3 rpm in order to maintain 15,750 scan lines/sec; these high speeds usually require pneumatic rather than mechanical bearings (Shepherd, 1991a) and make the polygon into a centrifuge that represents a significant safety hazard and that may need to be operated in a vacuum to avoid wind resistance and abrasion of the facets by atmospheric dust (Shepherd, 1991b). A vacuum housing then needs windows, which introduce additional optical surfaces and stray reflections. Finally, each facet of the polygon must be substantially larger than the beam diameter, since otherwise much of the duty cycle would be wasted whenever the beam straddles two adjacent facets.

Translating Concave Mirrors

Translation of multiple concave mirrors (Fig. 1) has been demonstrated in half-video-rate infrared scanning for military applications (Taylor, 1984). Scanning is achieved by rotating the disk, which translates the concave mirrors one at a time across the beam. Multiple identical concave mirrors are carved into the flat surface of a metallic disk by diamond micromachining. The optical design is too complex and ingenious to be summarized here; the interested reader should consult the original publication. However, application of the concept at visible or UV wavelengths is hindered by intrinsic aberrations and the imperfect smoothness of complex diamond-turned surfaces.

Resonant Galvanometers

Simple galvanometers (Montagu, 1991) can operate at the necessary scan rates if their waveform is simplified to be a pure sinusoid at the mechanical resonant frequency rather than a conventional sawtooth with all its high-frequency Fourier harmonics. Such devices (Fig. 1) are fairly cheap, extremely compact, optically simple, and achromatic, with high reflection efficiency at all λs and

Table 1. Comparison of Acoustic-optic Deflectors (AOD) and Resonant Galvanometers

Parameter	AOD	Resonant galvanometer
Scan rate	15.75 kHz sawtooth	7.875-kHz sine wave (requires digital rectification and linearization of pixel stream)
Synchronization to external clock	Easy	Difficult (galvanometer should be master oscillator)
Zoom possibilities	Needs optical corrections at high scan rates	Amplitude changes require 0.1–1 sec to stabilize
Random access	Yes	No
Chromatic dispersion	Yes (changing wavelengths is difficult, fluorescence descanning not possible)	No (pinhole confocality is no problem)
Compatibility with femtosecond pulses	Poor	Good
Optics	Difficult	Easy
Transmission or reflection efficiency	60% maximum	90–99%
Wear	No	No
Audible sound generation	No	Yes, needs muffling
Price including driver electronics	US $6000	US $3,000 not including scan rectification and linearization circuitry

negligible pyramidal errors or other variations from one scan line to the next. Scan angles are easily adjustable over a range well-suited to the acceptance angle of microscope objectives. Because the device is the rotational equivalent of a tuning fork, the mechanical motion does not cause any long-term wear. Of course, the resonant galvanometer does have disadvantages as well, mainly arising from the sinusoidal nature of the scan. The beam traverses the specimen in alternating directions, both of which must be used for efficiency's sake. Therefore, every other line is acquired in the wrong direction, and its order of pixels must be reversed electronically in order to be compatible with image processors and video equipment, which assume unidirectional scanning. Furthermore, the velocity of the scan is not uniform but rather cosinusoidal, fastest in the middle and slowest at either extreme. One solution is to use only the most central part of the scan, but the duty cycle is then inefficient and timing signals must still be provided to start each brief burst of data acquisition. The more satisfying solution is to use a large portion of the angular deflection and to acquire the pixels at intervals that are not uniform in time but correspond to equal spatial increments (Toyen, 1976; Montagu, 1991). A final minor nuisance is that a resonant galvanometer is a high-Q oscillator that cannot be effectively synchronized to an external frequency, because the slightest drift of the natural resonant frequency with respect to the external driving frequency would cause large changes in response amplitude and phase. Instead, a resonant galvanometer is customarily driven in a self-resonant manner, which makes it (rather than a quartz crystal) the master oscillator to which all other video components should be synchronized (Webb *et al.*, 1980).

The present authors believe that resonant galvanometers, though overlooked (Goldstein *et al.,* 1990) or considered too difficult to use (Draaijer and Houpt, 1988), are one of the most feasible ways of confocal scanning at video rates because of their superb optical and mechanical simplicity. Their drawbacks can be overcome by electronics whose complexity is only a minor tradeoff. The same conclusion was also independently reached by Nikon Corp. Acousto-optical deflectors simplify pixel acquisition and offer random-access scanning but can only attain slit confocality in the fluorescence mode and require careful automated optical corrections when excitation λs, scan rates, or scan amplitudes are changed. The following description will focus mainly on the instrument developed in the authors' laboratory at UCSD but will include some comparisons with the commercial systems from Nikon (resonant galvo-based) and Noran (AOD-based), which are discussed in later sections. Table 1 compares the advantages and disadvantages of the two scan techniques.

CONSTRUCTION OF A VIDEO-RATE, UV-VISIBLE LASER SCANNING CONFOCAL MICROSCOPY PROTOTYPE

Optical Layout

The optical layout of the UCSD experimental prototype is shown in Fig. 2. The entire system was constructed on a 2.5 × 8 ft vibration-isolated air table with post-mounted components for maximum ease of reconfiguration. Laser beams from 351 nm-514 nm from an Ar^+ ion laser, 543.5 nm from a He/Ne, or 700–900 nm from a pulsed Ti-sapphire laser are separately shuttered and made coincident by dichroic mirrors (not shown) and then enter the instrument from the left. The input beam passes through a spatial filter that also acts as a Keplerian beam expander so that the laser beam nearly fills the 5 mm pupil at the resonant galvanometer. A small fraction (<< 5%) of the intensity is then picked off by a beamsplitter, BS1, to serve as a positional reference beam to be described later. The main excitation beam is variably attenuated by a neutral density filter wheel and optionally stopped down by an iris to allow underfilling of the pupil and expansion of the diffraction-limited spot when so desired. The beam is then reflected 90° by the primary dichroic mirror, DM1. Wideband dichroic beamsplitters are more easily obtained when the short λ reflects and the longer λ transmits, rather than the reverse assignment. The beam then enters the scanner, consisting of a S-11108 resonant galvanometer and a G120DT linear servo galvanometer with a rectangular mirror (General Scanning, Watertown, MA). They are in close proximity without any relay optics between them. The resonant galvanometer mirror is 5 mm in diameter and was supplied with a resonant frequency of 8.0 kHz. We adjusted the frequency

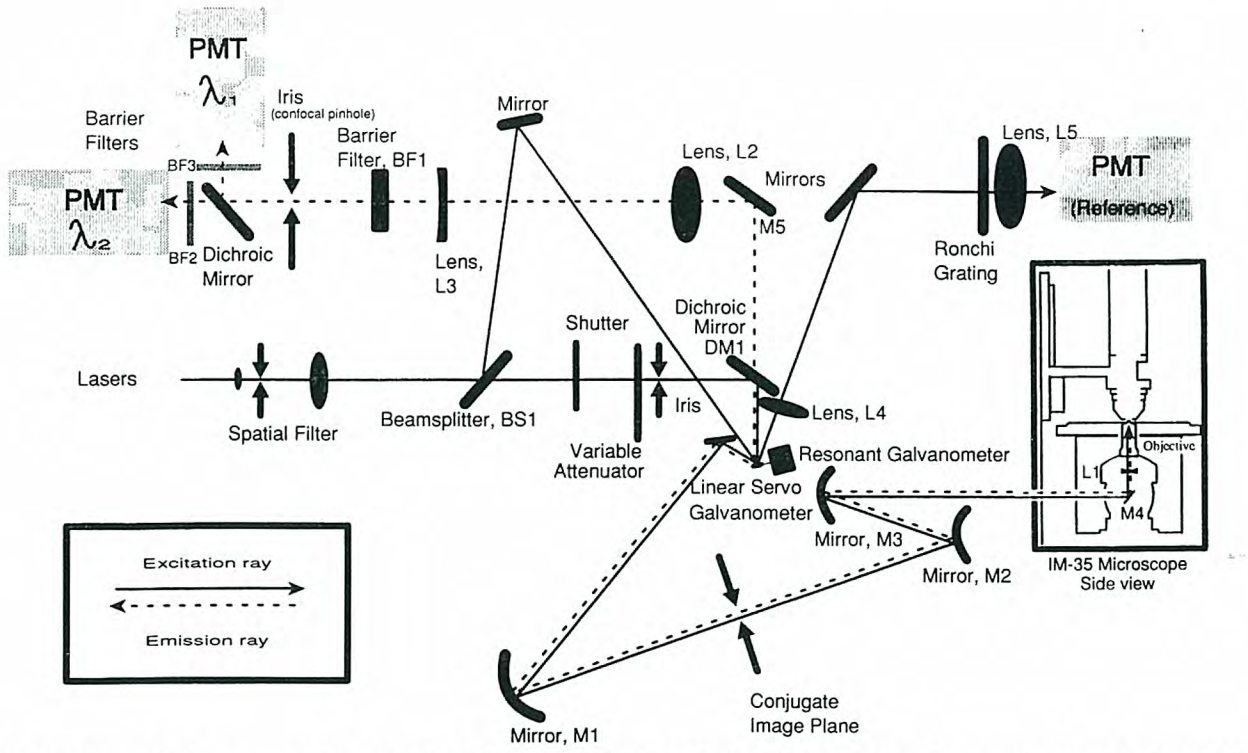

FIGURE 2. Optical layout for the prototype video-rate confocal microscope built at UCSD by the authors. A top view is presented, except at the lower right-hand corner, which is a side view of the IM-35 microscope stand. The excitation and emission paths are marked with solid and dashed lines, respectively. Curvatures and diameters of lenses and mirrors are not drawn to scale. The functions of most of the components are described in the text.

to 7.875 Hz by adding successive small increments of mass in the form of quick-setting epoxy applied to the nonmirrored back surface. Because each complete cycle gives two scans of opposite directions, the scan rate becomes 15.75 kHz as desired. The linear servo galvanometer is driven by a 60-Hz sawtooth phase-locked to the resonant galvanometer to generate the interlaced vertical scan.

The beam is then relayed into the microscope objective by a three-element telescope consisting of mirrors M1, M2, and M3. This telescope, designed by an optical consultant, Mr. Robert Sigler, is all-reflective in order not to contribute any chromatic aberrations and group velocity dispersion of laser pulses. It has a 3× magnification factor (viewed from the scanner end) so that the 5 mm resonant galvanometer would be conjugate to a 15 mm pupil at the microscope objective and is, therefore, not the limiting aperture. Of course, such 3× magnification means that the scan angle of the galvanometers must be increased threefold to about 3.3° peak-to-peak mechanical excursion, but such angles are well within their capabilities. An image plane is formed between the first and second mirrors, M1 and M2; the magnification from the specimen to this image plane is about 100×. This image plane is very useful because the unusable extremes of the horizontal and vertical scans can be blocked by adjustable masks placed here to prevent irradiation outside the desired measurement area. Furthermore, masks to restrict photobleaching or photactivation to arbitrary zones within the image frame can also be mounted here.

Finally, the excitation beam enters the inverted microscope stand, a Zeiss IM-35 inverted microscope, through the epifluorescence pathway, from which the usual lamp, condenser, iris, etc., have been completely removed and replaced by a hollow tube merely to exclude stray light. The Zeiss IM-35 was chosen because of its mechanical stability, stationary stage, fixed height of the epifluorescence optical axis and familiarity to the authors. The conventional epifluorescence filter cube of the Zeiss microscope contains no bandpass or cutoff filter but only a plane reflector, M4, to bend the beam 90° upward toward the inverted objective. When exciting with UV or visible λs, it is convenient to make M4 a dichroic mirror to reflect all λs below 700 nm, including both the excitation and emission, but passing conventional infrared (IR) trans-illumination from the specimen towards the eyepieces. When using two-photon IR excitation, the passband of the dichroic must be eliminated or moved to a different intermediate λ.

The nosepiece of the IM-35 microscope includes a quartz telan lens, L1, that converts conventional objectives of 160-mm tube length into an infinity-corrected objective. Therefore, no eyepiece is needed, and the collimated output of the telescope is appropriate for the composite objective. We have mostly used the Nikon 40×, NA 1.3 oil and 40×, 1.0 water-immersion objectives because of their high UV transmission, reasonable cost, and high NA and brightness (Table 2). Very recently the NA 1.0 water-immersion objective has been superseded by a Nikon 40×, 1.15 objective with even better properties. The field of view with a 40× objective was chosen to be 150 μm, corresponding to about 0.3 μm/pixel in both x and y directions with image dimensions of 512 × 486 pixels. We felt that a smaller field of view would give empty magnification and would be too small to encompass many cells of interest, whereas a larger field of view would sacrifice spatial resolution and invite problems from chromatic and other aberrations at the edge of the field of view. In conventional imaging with

40× objectives, 150 μm corresponds to about 30% of the field diameter visible through the eyepiece. Although yet smaller pixels might give somewhat finer spatial resolution (see Chapter 4, *this volume*), this prototype instrument was not designed to push the limits of spatial resolution for fixed specimens but to demonstrate high-speed imaging of diffusible ion indicators for which signal-to-noise considerations would already forbid very small volume elements.

The fluorescence emitted from the specimen is re-collected by the objective, collimated by the telan lens, relayed through the reflective telescope, descanned by the galvanometers and transmitted through the primary dichroic mirror, DM1. It is then deflected by a simple reflector, M5, and focused by a telephoto lens combination, L2 and L3, of 2500-mm effective focal length onto the confocal aperture, an adjustable iris diaphragm of 0.8- to 25-mm aperture diameter, corresponding to 0.53–17 μm at the specimen plane. The reflector M5 is necessary not only for compactness but to allow precise alignment of the emission beam onto the iris. The telephoto lens combination can be constructed from refractive elements, i.e., an achromatic convex lens, L2, and a simple plano concave lens, L3, since UV λs will not be present in the emission. The long effective focal length of the telephoto is required to give enough magnification, so that the macroscopic iris diaphragm corresponds to a reasonable range of spot sizes back at the specimen plane. After the emission has passed through the confocal aperture, it either falls directly on a photodetector or is split with a secondary dichroic mirror, DM2, into two λ bands, which impinge on two photodetectors mounted at right angles to each other. Additional barrier filters, BF1, BF2, and BF3, can be added as needed. Splitting the emission λs after rather than before the confocal pinhole economizes on components and eases geometric alignment but sacrifices the possibility of applying separate corrections for the chromatic aberrations at the two emission bands. So far, differential CA has not been severe, so a single pinhole configuration has been satisfactory.

The PMTs in current use are Thorn-EMI (Middlesex, England) 9658 photomultipliers with prismatic extended S-20 photocathodes for maximum quantum efficiency. The 50 mm diameter of these photocathodes means that no relay optics are required after the confocal aperture, even with the latter fully opened.

TABLE 2. Characteristics of Objectives Used with the RCM-8000 Video-Rate Confocal Microscope

Magnification	N.A.[a]	W.D.[b] (mm)	%T[c] (351 nm)	%T (488 nm)	λmax[d] (nm)	Corr. ring[e] (mm)
40 (oil)	1.3	0.22	64%	82%	656	—
40 (water)	1.15	0.20	56%	77%	768	0.14–0.2
60 planapo (oil)	1.4	0.17	—	80%	656	—
60 planapo (water)	1.2	0.22	—	80%	656	0.15–0.18

[a]Numerical aperture.
[b]Working distance.
[c]Percent transmission.
[d]Maximum wavelength for which correction of axial chromatic aberration is ensured. Yet longer wavelengths may be acceptable if chromatic aberration is unimportant or separately corrected.
[e]Range of thicknesses of glass cover slip that can be compensated by the correction collar.

Sensing the Resonant Galvanometer Position

The key to using a resonant galvanometer is to have accurate knowledge of its instantaneous angular position, in particular to generate a clock pulse whenever the beam traverses each evenly spaced pixel boundary from left to right or right to left. These clock pulses will not be evenly spaced in time. Because the angular velocity is greatest at the center of the scan, the clock pulses will be most frequent (spacing ~70 nsec) there and most infrequent (~160 nsec) at the left and right margins. If these clock pulses are used to trigger the A/D conversion of the photodetector outputs, then each pixel will represent an equal spatial displacement as desired.

The resonant galvanometer driver circuit does produce an analog voltage approximately representing its angular position. This 7.875-kHz sinusoid is phase-locked to the motion of the galvanometer and is, therefore, the motion signal from which horizontal and vertical sync must be generated. However, it is not accurate enough to be used to generate a pixel acquisition clock, especially when scans in opposite directions have to be registered to a fraction of a pixel interval, or within <0.1% of the scan duration. The analog sinusoid differs by a few degrees in phase from the displacement. If this sinusoid is passed through an analog phase-shifting circuit, it is adequate to drive a crude display on an analog *x-y* monitor, where the phase-adjusted resonant galvanometer output drives the *x*-axis, the position of the linear servo galvanometer drives the *y*-axis, and the signal PMT supplies the intensity modulation. Such an analog display is not recordable or quantifiable but is very simple and enables basic operation without an image processor. However, digital processing and recording requires a more precise pixel clock than can be obtained from the analog output of the resonant galvanometer.

We generate the pixel clock by optical sensing of the galvanometer position. A beamsplitter, BS1, extracts a few percent of the input laser intensity and directs this position-sensing beam onto the resonant galvanometer mirror but at a different angle of incidence from the main excitation beam. Both beams experience the same angular deflection, but the position-sensing beam misses the linear servo galvanometer and is instead focused by a lens, L4, onto a Ronchi grating consisting of alternating clear and opaque stripes of identical widths. The edges of the grating are masked so that **n** clear stripes are exposed. The principle is illustrated in Fig. 3, where for clarity **n** is only 8, but in the real grating **n** = 256. As the position sensing beam scans over the grating (cosine curve in Fig. 3), a PMT behind the grating receives **n** pulses of light (middle trace of Fig. 3). Each of the 2**n** transitions, whether dark to light or light to dark, is considered to indicate a new pixel to be acquired and is detected by a high-pass filter, comparator, and bidirectionally triggerable one-shot to generate a pixel clock pulse (bottom trace of Fig. 3). We prefer to detect both edges of each of the **n** clear stripes rather than one edge, say the left edge of each of 2**n** clear stripes, because the spatial frequency of the latter would approach the diffraction-limited angular resolution limit and because oppositely directed scan directions would require opposite trigger slopes. Typically, the **n** stripes span the central 90–95% of the peak-to-peak scan

amplitude, so that pixels are acquired for the middle 71–79% of the 63.5-μsec sweep duration.

Meanwhile, the outputs from the two emission-collecting PMTs are amplified by independent, high-speed, current-to-voltage converters, located within the PMT housings to minimize capacitance and susceptibility to interference. These amplifiers have a gain of 10 V/mA and a two-pole Butterworth response with their −3 dB cutoff frequencies at 4.5 MHz. The signals then pass through conventional video amplifiers with variable gain and offset and are digitized by 8-bit A/D converters triggered by the pixel clock generated from the Ronchi ruling. Thus A/D samples are acquired at equal spatial intervals, rather than equal temporal increments. The time increments between successive pixels range from about 70 nsec apart at the center of the sweep to about 160 nsec at the extremities. The nonuniform scan velocity must mean that the edges of the scanned area receive somewhat more light intensity than the center, but this effect is normally invisible on the resulting images. The PMTs are not looking at the specimen as an ordinary camera would, but instead view the flying zone of illumination. Unless the dye molecules in that zone are undergoing bleaching or ground-state-depletion during the dwell-time of the excitation beam, the instantaneous fluorescence intensity from that flying spot is independent of the scan velocity. The nonuniform scan velocity does mean that the left and right edges of the field of view may bleach somewhat faster than the center. Also, the fixed frequency bandwidth of the video amplifiers cannot be optimally matched to the variable sampling frequency both at the edges and the center. However, these imperfections are only of second-order importance and visibility. They also are counterbalanced by the usual tendency of optical systems to illuminate more brightly and resolve more finely at the center than at the edges of the field of view.

We do not attempt to do single-photon-counting at the A/D conversion stage because that technique becomes inaccurate and nonlinear at rates above about 10^7 s^{-1}, which would be about 1 photon/pixel at our scan rate. Digital photon-counting would therefore require restricting intensities to such low levels that tens to hundreds of sweeps would have to be accumulated to achieve a usable signal-to-noise ratio, negating the advantages of video-rate scanning. Even if photon-counting were feasible, it could only improve the final signal-to-noise ratio to a trivial extent in comparison to optimizing the transmission efficiency of the relay optics and quantum efficiency of the detector, avoiding illumination during retrace periods and minimizing analog noise from preamplifiers and PMT power supplies.

Signal Acquisition and Rectification

In order to rectify the bidirectional scan (Cohen-Sabban *et al.*, 1984), the digitized pixel brightnesses are stored in either a first-in-first-out (FIFO) or a last-in-first-out (LIFO) buffer, depending on whether acquired from left to right or right to left. The pixels acquired during one 63.5-μsec horizontal period, paced by the temporally nonuniform pixel clock, are played out during the following period at the uniform clock rate of the image processor. During any one horizontal sweep, one buffer is acquiring fresh data while the other is replaying the previous line. The overall pipeline delay is one horizontal line, or 63.5 μsec. The FIFO and LIFO buffers actually consist of static random-access memory chips addressed by counters. The FIFO address counter is reset to zero at the beginning of each horizontal line but always counts upwards, whereas the LIFO counts up during storage and down during playback. Two independent,

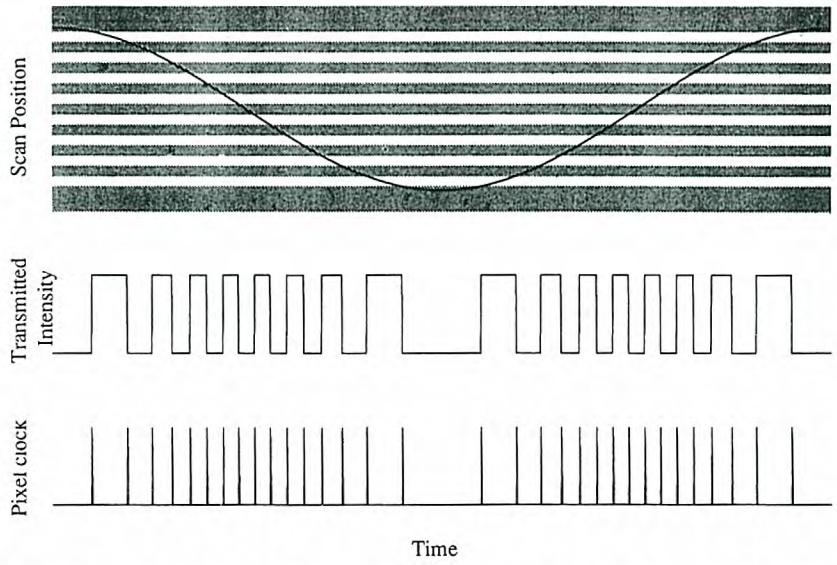

FIGURE 3. Schematic means for linearizing a sinusoidal scan. "Scan position" plots one complete cycle of cosinusoidal motion vs. time (127 μsec = full scale), superimposed on a Ronchi grating consisting of clear and opaque stripes of equal widths (top). For clarity, this example shows only 8 clear stripes, which span 95% of the peak-to-peak scan amplitude. The actual grating has 256 clear stripes and does not extend very far along the direction of the stripes because the actual beam constantly retraces a single line at right angles to the stripes and does not translate along the time axis. As the beam enters and leaves clear stripes, the transmitted light intensity detected by the reference PMT behind the grating rises and falls (middle). Each transition generates a pixel clock pulse (bottom) used to trigger analog-to-digital capture of the signals from the PMTs for emission λs 1 and 2. The pulses are nonuniformly spaced in time but correspond to equal intervals in image space.

identical FIFO/LIFO modules were custom designed and constructed, one for each input channel/wavelength range.

Video-Rate Image Storage

The image processor hardware was chosen for its ability to interface with the scan rectifier modules and perform the following simultaneous functions: average the images arriving on two independent channels at 30 frames/sec, store the two averages (one for each channel) in interleaved fashion (up to 15 pairs/sec) on a single monochrome optical-memory disk recorder (OMDR), and display their arithmetic mean and log ratio as pseudocolor brightness and hue in a continuous real-time display. These functions were considered essential for fast physiological experiments with emission-ratioing indicators such as Indo-1, fura-red/fluo-3 mixtures, or the cAMP indicator FlCRhR. The reasons are the same as previously explained for excitation ratioing in conventional microscopy (Tsien and Harootunian, 1990). The two input channels representing different λ bands should be stored as distinct monochrome images to retain maximum spatial resolution and to permit later reprocessing, for example with different background subtractions or a different mapping between ratios and pseudocolors. Such storage, which needs to handle 7.5 Mbytes/sec for up to several minutes at a time, is beyond the capacity of video memory but could be accommodated by very-high-speed digital disks, OMDRs, or videotape recorders. Digital disks that can handle real-time video are currently extremely expensive per megabyte stored and require elaborate and frequent backup onto digital optical disks or magnetic tape. Experience shows such backup to be tedious and error-prone on a routine basis. Videotape is very cheap but sacrifices random access to specific selected frames. The OMDR needs no backup and is a good compromise between cost, speed (30 frames/sec), capacity (tens of thousands of images on a single disk), image quality and random access. However, we wished to record two channels yet avoid the expense of buying two OMDRs, the inconvenience of coordinating pairs of disks for each playback, and the possibility that two units could develop mismatches in analog offset or gain, or pixel-by-pixel synchronization. Therefore, a twofold compression of data is required to fit the two channels onto the single device. Currently, this compression is accomplished by averaging two successive 33 msec frames from each channel and then storing the two averages as pairs of 33 msec frames on the OMDR while simultaneously averaging the next two input frames on each channel (Fig. 4). Averaging successive frames lowers the time resolution to a maximum of 15 ratio images/sec, but such averaging would usually be required to improve the signal-to-noise ratio in any case. A real-time display of the ratio is very helpful, so that

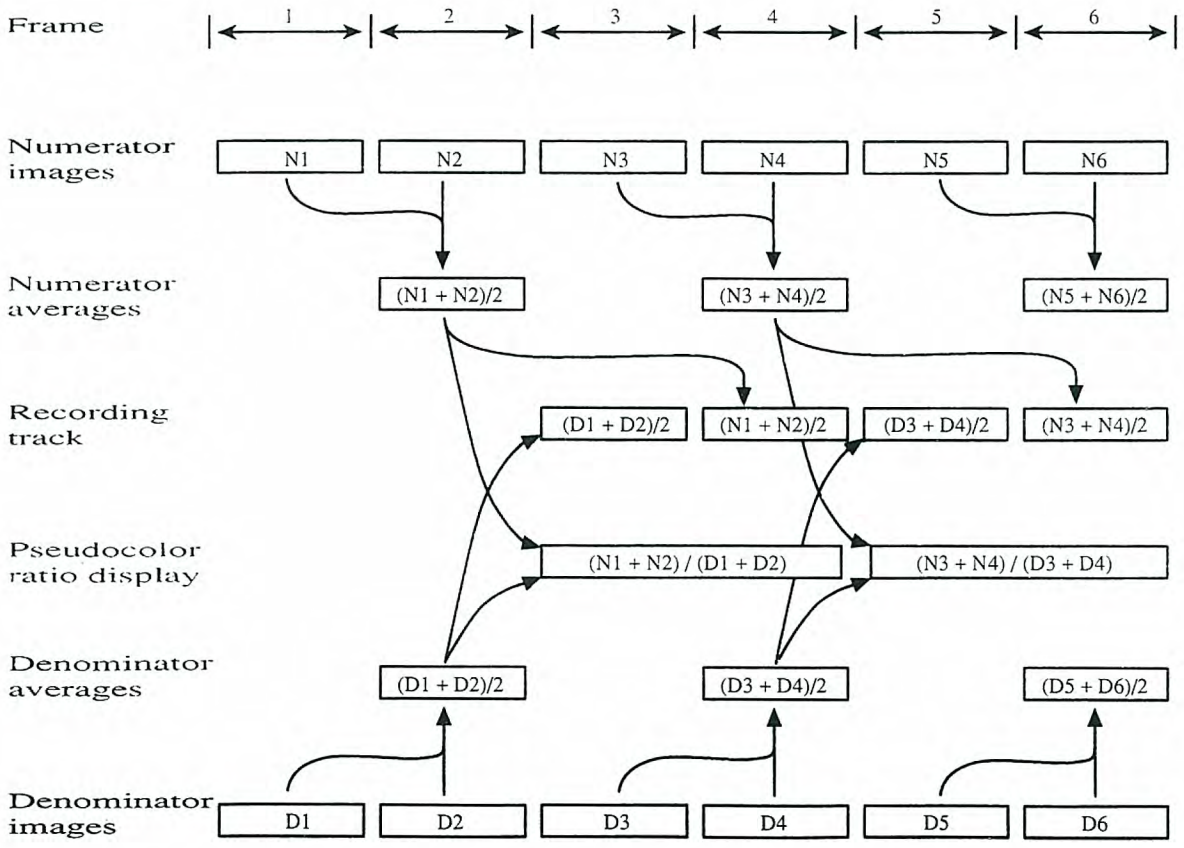

FIGURE 4. Timing diagram for simultaneous acquisition, storage, and ratio display of two video input channels. The horizontal axis represents time in units of video frames, normally 33.3 msec each. Sequential input frames on the numerator and denominator channels are individually labeled on the top and bottom tracks. Successive pairs of frames are averaged and sent to the optical memory disk recorder (OMDR or "recording track") one or two frames after computation. For historical reasons, the denominator is stored before the numerator, but this ordering is arbitrary. Meanwhile, the ratio of the numerator and denominator is displayed in pseudocolor during the 67-msec period following the acquisition of its constituents.

the progress of the experiment can be gauged while there is still time to influence it. Even while one is scanning the tissue for suitable cells, on-line ratioing shows which cells have healthy, low Ca^{2+} levels vs. pathologically high values.

Image Processor Hardware and Software

Our implementation of the above requirements was constructed (starting in 1988) from MaxVideo-10 boards from Datacube, Inc. (Danvers, MA). This system was chosen because its components are completely modular and easy to patch together via external digital video buses whose specifications are published. Thus the home-made input modules could easily simulate Datacube devices. Figure 5 shows block diagrams of how averaging, storage and ratio display are simultaneously accomplished at maximum speed with a relatively small number of components and frame memories. The read and write ports of the memories are set up so that readout of each stored pixel occurs just before new data overwrites it, so that in each frame time, a memory plays back a previously stored image and can optionally be updated by a new image. Figure 5A-D represents successive 33-msec frames corresponding to phases 1, 2, 3, and 4 of Fig. 5. In Fig. 5A, the first frames from denominator and numerator λs are simply stored in memories 1 and 2. In Fig. 5B, the stored frames are added to the incoming new frames and divided by 2 to form the 8-bit averages. These are not only re-stored in memories 1 and 2 but also passed as high- and low-input bytes to the 16-bit× 16-bit lookup table. As detailed in the inset to Fig. 5B, this table has been pre-loaded by the host program to generate the appropriate 8-bit output pseudocolor code for every possible combination of 8-bit numerator and 8-bit denominator, including 3 bits of mean intensity and 5 bits of log ratio. Spatially uniform background levels N_0 and D_0 for the numerator and denominator can be deducted before ratioing, simply by programming the lookup table appropriately. The remaining 8 bits of the 16 possible output bits are simply a replica of the input numerator. The pseudocolor and replicated numerator are then stored in the lower and upper bytes of frame store 0. The reason for replicating the numerator via the lookup table is to maintain the identical pipeline delay between the pseudocolor and the numerator and keep them in exact register. Figure 5C is identical to Fig. 5A, except that the previously stored average denominator is displayed to the OMDR just before it is wiped out by the new incoming data. Also, the pseudocolor brightness-modulated log ratio is displayed to the user by a separate digital-to-analog RGB output. Figure 5D is identical to Fig. 5B, except that the previously stored average numerator is displayed to the OMDR just before it is wiped out by the new average numerator, and the pseudocolor is displayed as in Fig. 5C. Thus, the pseudocolor ratio calculated from any given 67 msec period is displayed to the user during the following 67 msec. The above process can be easily slowed down if more than two frames are to be averaged or if gaps are to be inserted. When high speed is not essential, additional steps can be added to correct for nonuniform backgrounds and shading. For post-experimental analysis, images played back from the OMDR are sequentially digitized by a conventional frame-grabber board and re-processed.

When only a single λ is being acquired, as with nonratiometric indicators, acquisition, storage and display at up to 30 frames/sec is trivial. Ratioing against an initial prestimulus image is likewise easily accomplished by preloading and freezing it in the denominator frame buffer while the lookup table computes its ratio with respect to the changing numerator at 30 frames/sec.

Because the image computation is performed by the pipeline processor boards from Datacube, the host CPU does not need to be very powerful; even a Motorola 68020 is adequate. However, it is helpful to use a real-time operating system with fast response to interrupts at the beginning of each frame so that the control registers of the Datacube system can be reset during vertical blanking. Therefore, the Unix-like but real-time system OS-9 (Microware, DesMoines, IA; not to be confused with OS/2 from IBM) was selected. A large suite of C language programs has been written, mostly mimicking the capabilities of previous systems for ratio imaging (Tsien and Harootunian, 1990) but adding such features as collection of *z*-series, rapid switching between visible and UV lasers for photostimulation or uncaging, interfacing with electrophysiological stimulus generators, and signal-averaging of image sequences acquired in response to repetitive stimuli.

COMMERCIAL RESONANT-GALVANOMETER-BASED VIDEO-RATE CONFOCAL MICROSCOPY: NIKON CORPORATION RCM-8000

The above technology developed in the author's laboratory was licensed by the University of California to Nikon Corporation, which had already independently begun to develop a video-rate confocal microscope based on a resonant galvanometer. The first commercial units, model RCM-8000, use quite different optical relay systems (Fig. 6) from the author's but similar electronics, image processor configuration, and software. Nikon's optics have been computer-optimized as an integrated system including the detailed properties of the objectives and are much more compact and stable but, of course, much less easily reconfigurable than the author's prototype. One interesting difference is that the Nikon system senses the resonant galvanometer position by bouncing a diode laser beam off the reflective back surface of the resonant galvanometer. Such an independent reference beam eliminates the need to readjust the reference beam optics when changing excitation laser λs. Resonant galvanometers with reflective surfaces on both front and back were unavailable when the UCSD system was under construction.

PERFORMANCE TESTS

Resolution

Currently there are few if any accepted criteria for the performance of a confocal microscope, especially when trying to separate the properties of the microscope objective from the rest of the system. One easy and frequently used test is to focus towards and away from a plane mirror and determine the *z*-axis width of the response peak. Unfortunately, this tests coherent reflection rather than incoherent fluorescence and seems very remote from typical biological specimens. Our preference for an all-round test of 3D resolution is to image diatom skeletons immersed in a solution of fluorescent dye. The skeleton of any particular species of diatom is a complex silica meshwork of highly stereotypic anatomy, with a whole hierarchy of ribs, spines, and knobs ranging in size from tens to hundredths of microns. Diatoms have long been favorites

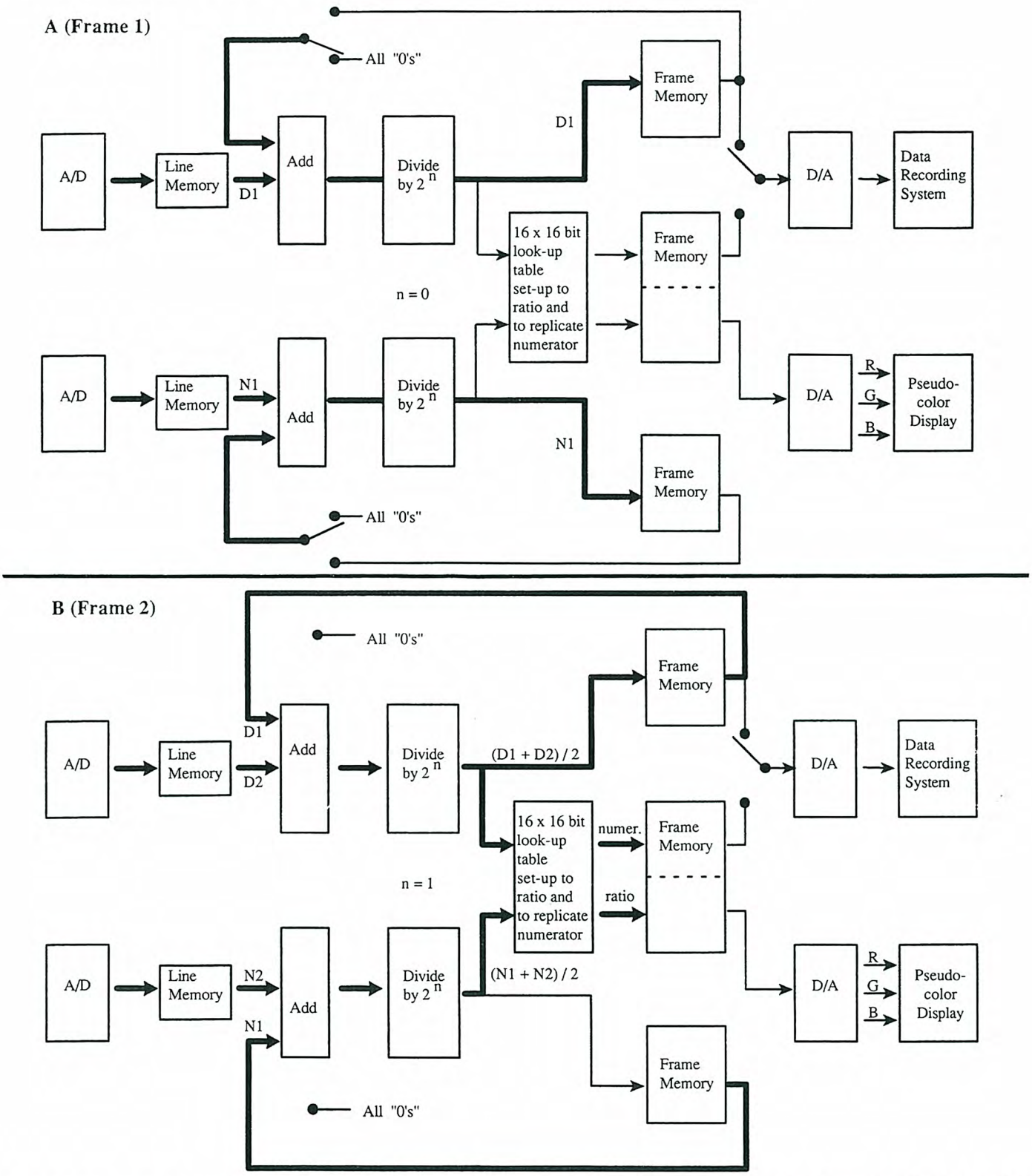

FIGURE 5. Image processor operations during acquisition, storage, and ratio display of two video input channels. Heavy lines show active signal paths, each 8 bits wide except 16 bits between the add and divide-by-2^n circuits. (A-D) Operations during frames 1–4, respectively, as defined in Fig. 4. Subsequent frames repeat C and D. The "line memories" just after the A/D converters contain the first-in-first-out and last-in-first-out buffers to rectify the scan and re-transmit pixels at a uniform clock rate. All three frame memories are 16-bits deep, though the upper 8 bits of the memories dedicated to numerator and denominator remain unused when only two successive frames make up each average. Switching between data paths is accomplished by solid-state multiplexer circuits rather than physical toggling.

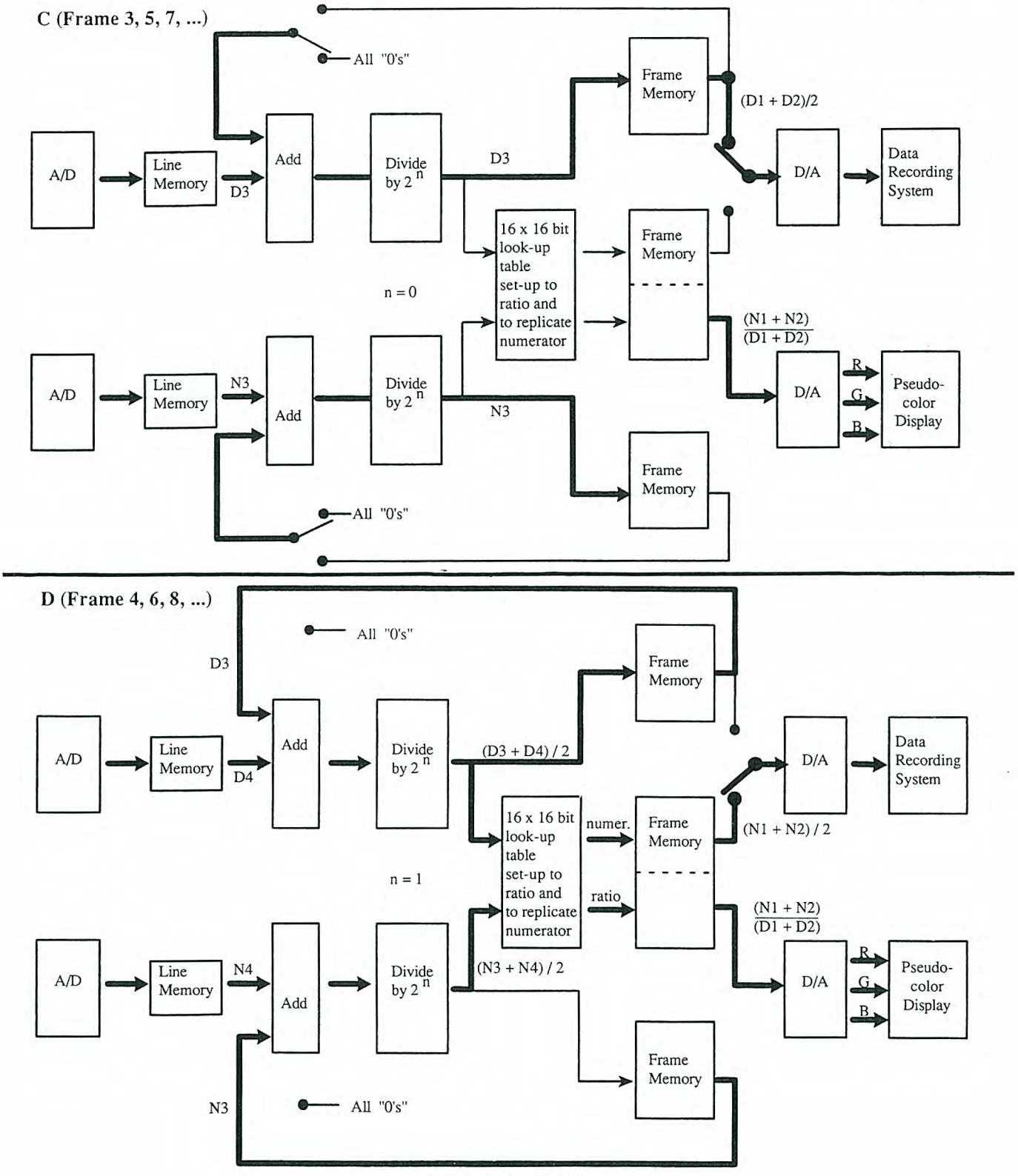

FIGURE 5. (*Continued*)

for testing the resolution of conventional transmitted-light microscopy. They are equally useful for confocal fluorescence microscopy, once immersed in a fluorescent solution. The skeleton then becomes a negative specimen, which is stable against photobleaching because it is made of silica interspersed with dye that is continually replenished by diffusion from the nonilluminated volume. Because fluorescence comes from all the immediate neighborhood of the diatom, there is a huge amount of out-of-focus signal that must be rejected. The quality of confocal sectioning is tested much more stringently with such negative specimens rather than

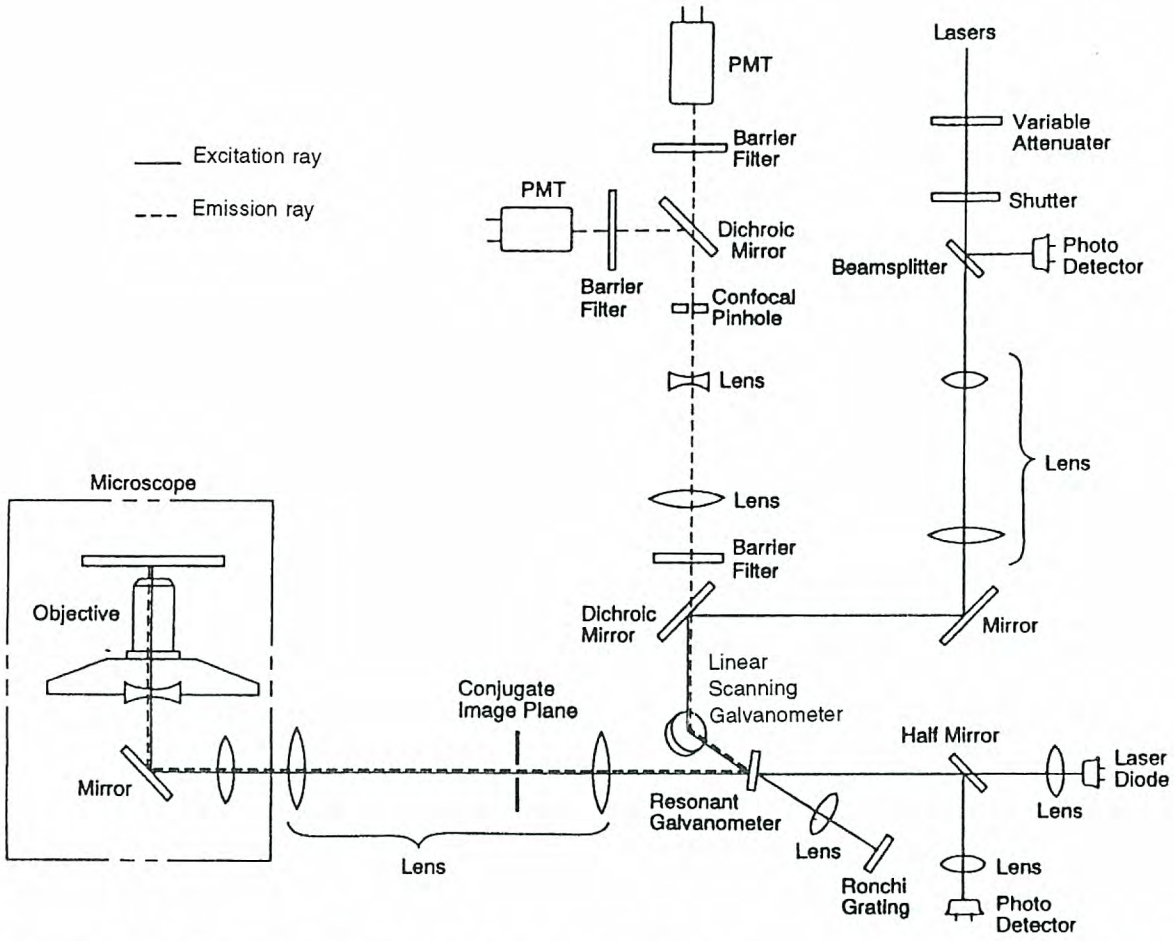

FIGURE 6. Optical layout for the Nikon RCM-8000 video-rate confocal microscope. The entire diagram is a top view, except for the inset labeled Microscope, which is a side view.

targets giving positive signals such as fluorescent beads or sparsely stained immunofluorescence sections, which are often too "easy" in the sense that mere simple high-pass spatial filtering is often sufficient to make the images look very good. Any fluorescent dye at any concentration in any solvent can be used, so that images from diatoms of closely reproducible morphology can be compared while varying the λ, signal strength, and refractive index at will. Finally, diatoms are cheap, readily available, indefinitely stable, and portable. In our sample of mixed diatoms, the most spectacular skeletons are from *Epithemia turgida* (Round *et al.,* 1990; Sims, 1983), and the smallest and most difficult details to image are the fine cross struts about every 1.5 μm linking the stouter transverse ribs. The spacing between those ribs is about 3 μm. Figure 7 shows three *E. turgida* skeletons immersed in 7-hydroxycoumarin (for UV excitation at 351 nm), fluorescein (for blue excitation at 488 nm) and rhodamine B (for green excitation at 543.5 nm). All the dyes were at 1 mM in aqueous solution (pH 9 for the 7-hydroxycoumarin and fluorescein) and were viewed with an RCM-8000 with a newly developed water-immersion 40×, NA 1.15 objective (Table 2). Slightly better images can be obtained with dyes dissolved in immersion oil and viewed with an oil-immersion objective (not shown), but imaging in aqueous media is more challenging and more relevant to live tissues.

Live Cell Ca^{2+} and cAMP

In most real biological specimens, unlike the above diatoms, photobleaching and photodynamic damage are severe constraints. Test specimens should have interesting 3D fine structure (unlike fluorescent beads) decorated with controllable and easily reproducible amounts of bleachable dye; the challenge (ideally issued to all manufacturers) would be to get the best possible images from the lowest amounts of dye before they bleached completely. We are not aware of such specimens, although they could almost certainly be developed. Instead, we have concentrated on imaging live cells doing interesting physiology. Although such images are not quantifiable measures of instrument quality, they at least may be representative of real biological applications, which are the ultimate test. Heart muscle cells, either acutely dissociated adult or cultured neonatal, are particularly suitable because they readily generate repetitive Ca^{2+} waves that rapidly propagate throughout the cell, often accompanied by visible motion (see for example Takamatsu and Wier, 1990; Niggli and Lederer, 1990). Moreover, their biological significance is easily understood even by engineers and business executives. Figure 8 shows a neonatal cardiac myocyte, loaded with the Ca^{2+} indicator Indo-1 via its acetoxymethyl ester, imaged at 15 ratios/sec with 351 nm excitation while viewing

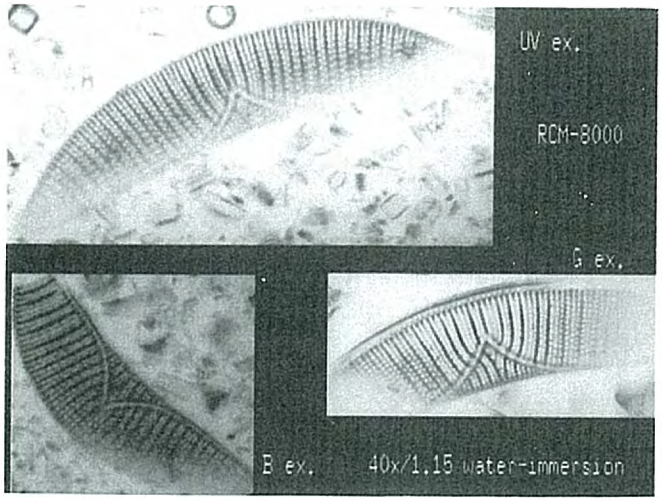

FIGURE 7. Confocal sections through diatom skeletons immersed in fluorescent dye solutions. Diatomaceous earth (catalog no. PB115, Carolina Biological Supply) was slurried with aqueous solutions of fluorescent dyes. Skeletons of *Epithemia turgida* were selected for view because of their size and feature-richness, but many smaller diatoms and fragments are also visible. Other sources of diatomaceous earth, particularly chemical grades intended for filtration, are often so highly pulverized as to contain no recognizable skeletons. The best source would, in principle, be skeletons derived from diatom monocultures. Labels UV ex., B ex. and G ex. indicate excitation of 7-hydroxycoumarin at 351 nm, fluorescein at 488 nm, and rhodamine B at 543.5 nm, all at 1 mW. The coumarin and fluorescein were in borate buffer at pH 9 to ensure complete ionization of their phenolic protons. A Nikon 40×, NA 1.15 water-immersion objective was used on a Nikon RCM-8000 system.

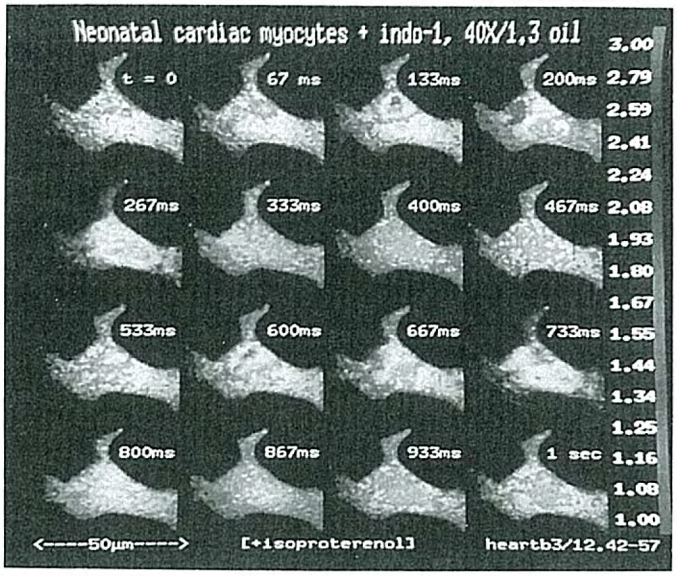

FIGURE 8. Repetitive waves of cytosolic Ca^{2+} in neonatal cardiac myocytes viewed by emission ratioing of Indo-1. Neonatal heart muscle cells were loaded with the emission-ratioing Ca^{2+} indicator Indo-1 by incubation with Indo-1/AM and stimulated with 10 µM isoproterenol as a positive inotropic agent to amplify the cells' tendency to generate $[Ca^{2+}]_i$ transients. Excitation was at 351 nm. Emission λs bands of 390–440 and >440 nm were separately acquired at video rate and stored at 15 ratio pairs/sec just as described in Figs. 4 and 5. The interval between each image is therefore 67 msec. Pseudocolors from blue to red indicate increasing ratios of 390–440 to >440 nm emissions, which signal increasing values of cytosolic Ca^{2+}. (See color insert facing page 472 for color version.) The color scale is calibrated in terms of ratios normalized to 1.0 for Indo-1 in EGTA medium with 0 Ca^{2+}. These 16 images were arbitrarily selected from a continuous series of 1129 and have been spatially smoothed by a convolution with a 3 × 3 kernel. Only one small portion of the field of view has been included in this montage; an approximate distance scale is shown at the lower left. The cells were prepared by Drs. Hikaru Tanaka and Koki Shigenobu of Toho University and imaged with a 40×, NA 1.3 objective on a Nikon RCM-8000 by Drs. Toru Kawanishi and Chikako Uneyama of the National Institute of Hygienic Sciences, Japan, and one of the authors (RYT).

simultaneously at violet and blue λs. Two complete cycles of Ca^{2+} oscillation propagate in a reproducible spatial pattern from a fixed locus in slightly less than one sec. The dye concentration was clearly not too high, or else oscillations would have been prevented. At the level of illumination used here, the half-life of the dye was about 1,000–2,000 images each of 1/15 sec; only 16 frames are shown here. In a real experiment, one would probably not illuminate continuously at this rate but would open the shutter only for selected periods. For most types of experiments, 1,000 images would probably be sufficient. For comparison, Fig. 9 shows an analogous myocyte loaded with the visible but nonratiometric indicator fluo-3, imaged at 30 frames/sec (no averaging) with 488 nm excitation while collecting the entire green emission band. Because only one λ channel needed to be stored to the OMDR, the time resolution could be twice as good. The monochrome intensity changes are quite dramatic when the images are played back as a continuous sequence but are hard to see in a static montage, so the images have been pseudocolored by ratioing each against an arbitrary initial image defined as time zero. Again, very small regions of initiating high Ca^{2+} are readily apparent. The failure of the region at the upper right corner of each panel to brighten very much is probably due to local overload of the A/D converter. About 3,000 images of 1/30 sec could be collected with only minor bleaching overall. Fluo-3 is probably superior for qualitative observation of where and when Ca^{2+} is elevated, as the rate of image storage can be twice as high as with Indo-1, yet the bleaching rate is lower. However, Indo-1 will be superior whenever absolute levels of $[Ca^{2+}]_i$ are of interest, since ratioing makes calibration very much easier.

Two-photon excitation (see Chapter 28, *this volume*) with femtosecond pulses of IR offers several important potential advantages over one-photon excitation with UV or blue light. IR is much better at penetrating tissue and minimizing damage: CA problems are reduced when UV is eliminated; descanning and confocal detection are no longer necessary; and dye outside the plane of focus is not even being excited, so bleaching and dye-related photodynamic damage are minimized. As pointed out by Denk in Chapter 28, only point scanning of a laser by real mirrors can achieve the extremely high local photon fluxes required for two-photon excitation. Scanners based on resonant galvanometer mirrors should be the most direct way to achieve two-photon excitation at video rates. Figure 10 confirms the feasibility of this combination. Astrocytoma cells loaded with Indo-1 are imaged with ~720-nm pulses from a Ti–sapphire laser. Elevation of $[Ca^{2+}]_i$ by application of glutamate is clearly visible. Technical problems with our relatively crude Ti–sapphire laser make two-photon excitation

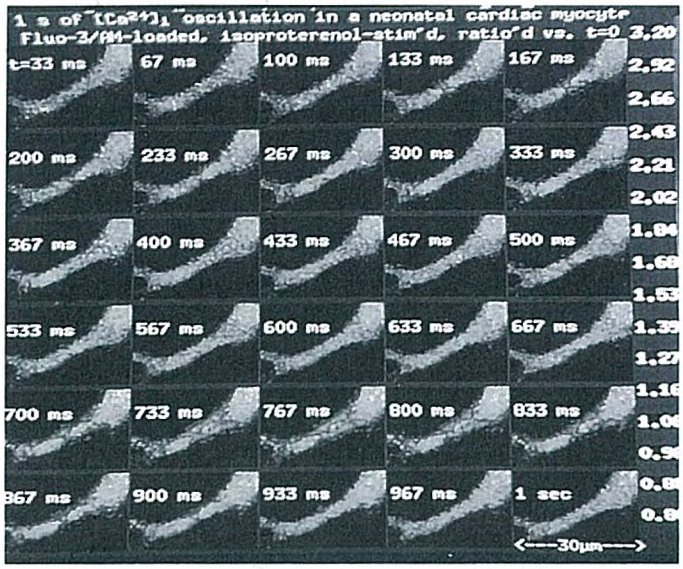

FIGURE 9. Repetitive waves of cytosolic Ca^{2+} in neonatal cardiac myocytes viewed by ratioing fluo-3 images against a fixed initial image. Cells were prepared and viewed as in Fig. 8, except that loading was with 10 μM fluo-3/AM, excitation was at 488 nm, and a 40×, NA 1.15 water-immersion objective was used. The fluorescein emission band (>510 nm) was acquired and stored at 30 frames/sec, so that the interval between each image is 33.3 msec. To help the eye distinguish changes in intensity that are easy to see as a continuous video sequence but difficult to discern when placed side by side in a static montage, each image has been ratioed against an arbitrary frame defined as $t = 0$, acquired just before the first frame actually shown ($t = 33$ msec). The $t = 0$ frame was an approximate trough in the repetitive $[Ca^{2+}]_i$ oscillations, so that most of the subsequent frames show higher intensities, ratios and $[Ca^{2+}]_i$ values. The color scale on the right is calibrated in units of ratio with respect to the $t = 0$ image; calibration in terms of absolute $[Ca^{2+}]_i$ levels is difficult because of the nonratiometric response of fluo-3. (See color insert facing page 472 for color version.) The failure of the region at the upper right corner of each panel to brighten very much and reach a high ratio is probably due to local overload of the A/D converter. These 30 images were arbitrarily selected from a continuous series of 3,103 images and have been spatially smoothed as in Fig. 8. An approximate distance scale is shown at the lower right.

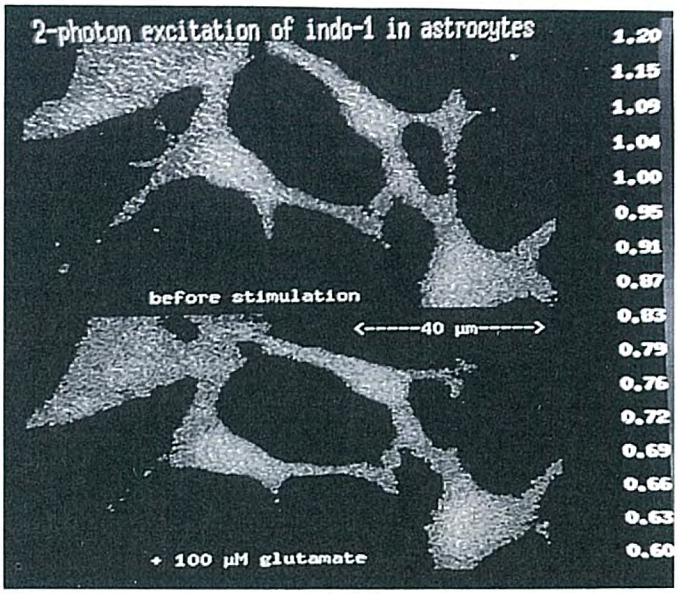

FIGURE 10. Two-photon excitation of Indo-1 in cultured astrocytes. Primary cultures of neonatal rat brain astrocytes were plated on glass coverslips and maintained for ≤2 weeks. Coverslips were loaded with 1 μM Indo-1/AM for 1 hr and observed on the stage of the UCSD confocal microscope. Excitation was accomplished with a mode-locked Ti–sapphire laser (NJA-3, Clark Instrumentation) operating at about 100 mW average power at around 720 nm. This λ was the lowest that the NJA-3 could produce but is still somewhat too high for Indo-1, whose Ca^{2+} complex is only weakly excitable by pairs of 720 nm photons. Emission λs of 380–440 nm and >440 nm were collected simultaneously, and a ratio image was calculated and displayed in pseudo-color. (See color insert facing page 472 for color version.) The color scale at the right of the images represents (380–440):(>440 nm) ratios, not concentration of intracellular calcium. (top) Resting fluorescence ratios in a group of cells before stimulation. (bottom) Increase in ratio resulting from addition of 100 μM glutamate. When the laser was not mode locked, no fluorescence could be detected.

less convenient and sensitive than conventional UV excitation, but this status should change as the pulsed lasers improve.

Recently there has been increasing interest in the prospect of monitoring Ca^{2+} changes not in the cytoplasm as in the above images but in specific organelles. For example, the Ca^{2+}-sensitive chemiluminescent protein aequorin has been fused with a leader sequence from cytochrome oxidase to target the fusion protein to the mitochondria (Rizzuto *et al.,* 1992). Unfortunately, aequorin signals are difficult to image at high spatial resolution because of the very limited number of photons generated by chemiluminescence. Confocal microscopy of chemiluminescence is impossible because excitation light is unwanted. Can fluorescent indicators for Ca^{2+} be targeted to the mitochondria? Rhod-2/AM preferentially loads mitochondria (Minta *et al.,* 1989) because all the carboxylate negative charges are masked by the acetoxymethyl esters, leaving only the delocalized positive charge on the rhodamine, which promotes uptake into mitochondria because of their deep negative membrane potential. Once the esters are hydrolyzed, the trapped dye reports increasing intramitochondrial Ca^{2+} as increased brightness. Confocal images of rhod-2 excited with the 543.5 nm line of a greenHe/Ne laser are shown in Fig. 11. In resting fibroblasts (Fig. 11A), the fluorescence is already largely punctate. Addition of vasopressin to elevate cytosolic Ca^{2+} in these cells causes a rapid brightening of the mitochondria (Fig. 11B), showing that they immediately begin taking up Ca^{2+} from the cytosol, just as seen with mitochondrial aequorin in bovine endothelial cells. However, as the transient cytosolic Ca^{2+} spike decays, the Ca^{2+} leaves most of the mitochondria, confirming that Ca^{2+} uptake is rapidly reversible. Interestingly, a few organelles, particularly around the periphery of the cell, tend to stay bright (Fig. 11C), perhaps indicating heterogeneity of cytosolic Ca^{2+} values or mitochondrial properties. The ability to watch individual organelles is a particular strength of confocal microscopy. Finally, additional staining with the relatively mitochondria-specific probe rhodamine 123 (Fig. 11D) brightens the same organelles, confirming that the rhod-2 signal comes largely from the mitochondria. Another control is that the mitochondrial uncoupler FCCP should short-circuit the membrane potential and release the sequestered Ca^{2+}. FCCP does indeed rapidly eliminate the punctate brightness (not shown).

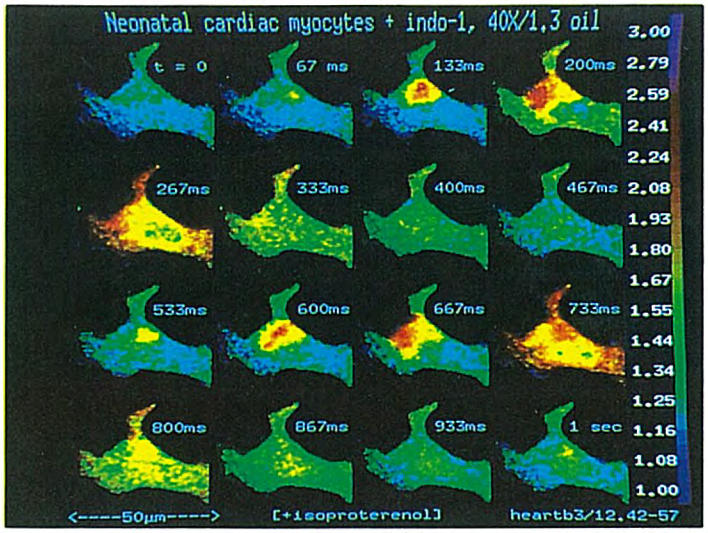

FIGURE 29.8. Repetitive waves of cytosolic Ca^{2+} in neonatal cardiac myocytes viewed by emission ratioing of Indo-1 in 16 images @ 67 ms intervals. Cells, loaded via incubation with Indo-1/AM, were stimulated with 10 µM isoproterenol to amplify normal $[Ca^{2+}]_i$ transients. $\lambda_{excit.}$ = 351 nm. $\lambda_{emit.}$ bands at 390–440 and > 440 nm were acquired separately at video rate. Pseudocolors from blue to red indicate increasing ratios and increasing cytosolic Ca^{2+}. The images selected represent only part of the field of view and have been spatially smoothed with a 3 × 3 kernel. 40×/1.3 objective on a Nikon RCM-8000. *See also* page 471.

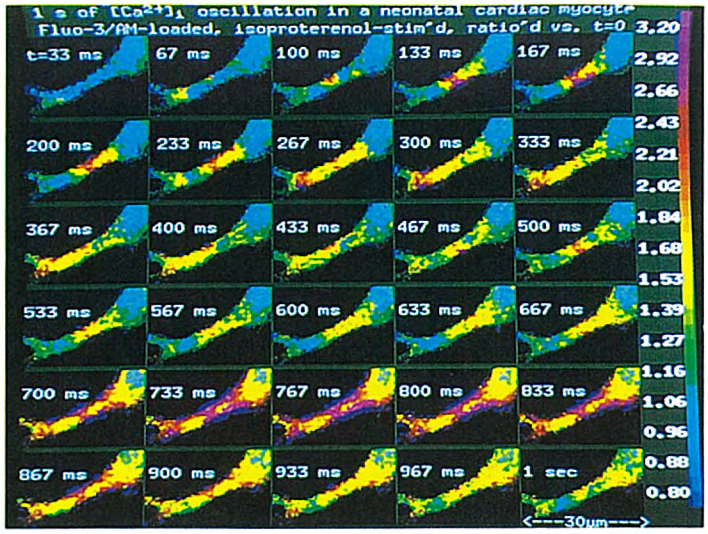

FIGURE 29.9. Repetitive waves of cytosolic Ca^{2+} in neonatal cardiac myocytes viewed by ratioing fluo-3 images against an earlier, reference image. Cells prepared and viewed as in Figure 8 but loaded with 10 µM fluo-3/AM, $\lambda_{excit.}$ = 488 nm, $\lambda_{emit.}$ = 510 nm, a 40×/1.15 water objective was used, and images were stored at 30 frames/sec and selected and smoothed as in Figure 8. The reference image was acquired at a trough in the $[Ca^{2+}]_i$ oscillations just before the first frame actually shown. The color scale on the right shows ratios to this reference image. *See also* page 472.

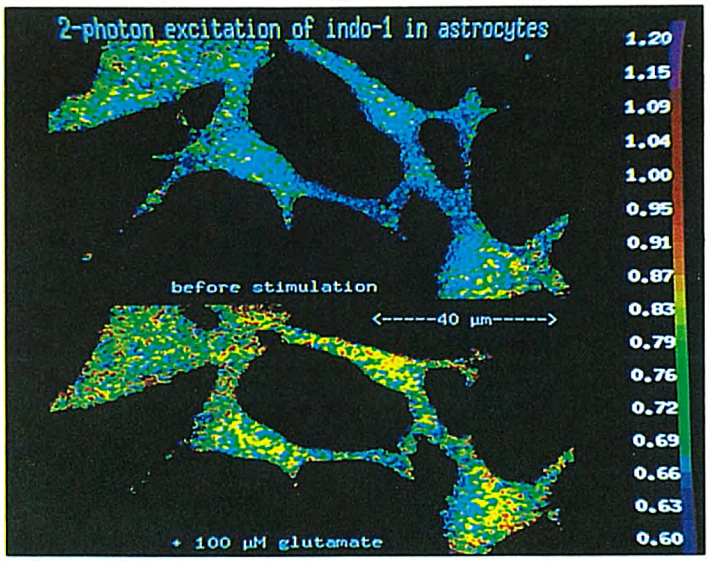

FIGURE 29.10. Two-photon excitation of Indo-1 in cultured astrocytes. Coverslips were loaded with 1 µM Indo-1/AM for 1 hour and observed on the stage of the UCSD confocal microscope. Excitation at $\lambda_{excit.}$ = 720 nm, $p_{average}$ = 100 mW, with a mode-locked Ti:sapphire laser (NJA-3, Clark Instrumentation). $\lambda_{emit.}$ bands were collected simultaneously at 380–440 nm and > 440 nm, and a ratio image was calculated and displayed in pseudocolor. The top panel shows resting fluorescence ratios in a group of cells, and the bottom panel shows the increase in ratio resulting from addition of 100 µM glutamate. Fluorescence could not be detected unless the laser was mode-locked. *See also* page 472.

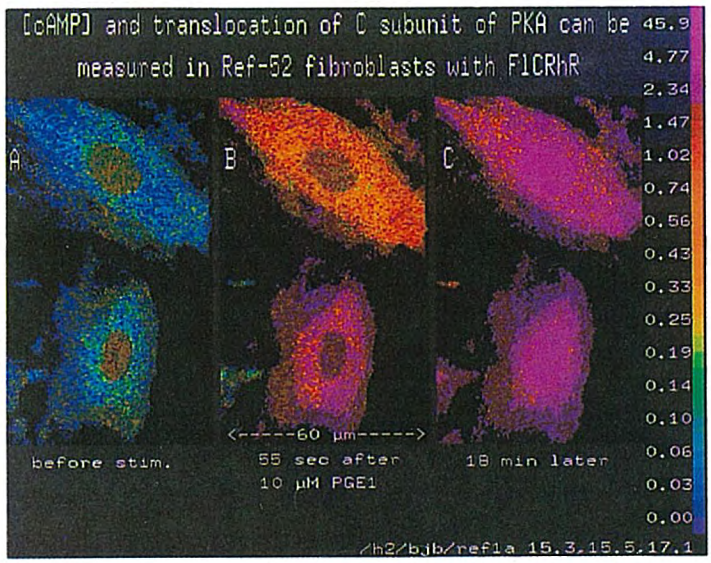

FIGURE 29.12. Imaging of [cAMP] and of subunits of labeled PKA in single cells. REF-52 fibroblasts were pressure-injected with $FlCRhR^{II}$ and imaged on the UCSD confocal microscope at 488 nm. $\lambda_{emit.}$ bands at 510–545 nm for fluorescein and > 560 nm for rhodamine were ratioed in real time and displayed as pseudocolors. The two cells in (A) exhibit low-resting [cAMP] values and nonfluorescent nuclei. (B) was made 1 minute after stimulating the cells with 10 µM PGE_1, raising [cAMP] to high levels. (C) is 17 minutes later, and [cAMP] in both cells is still at saturated levels (> several µM), but the C subunit has had time to enter the nuclei, which are no longer dark. *See also* page 473.

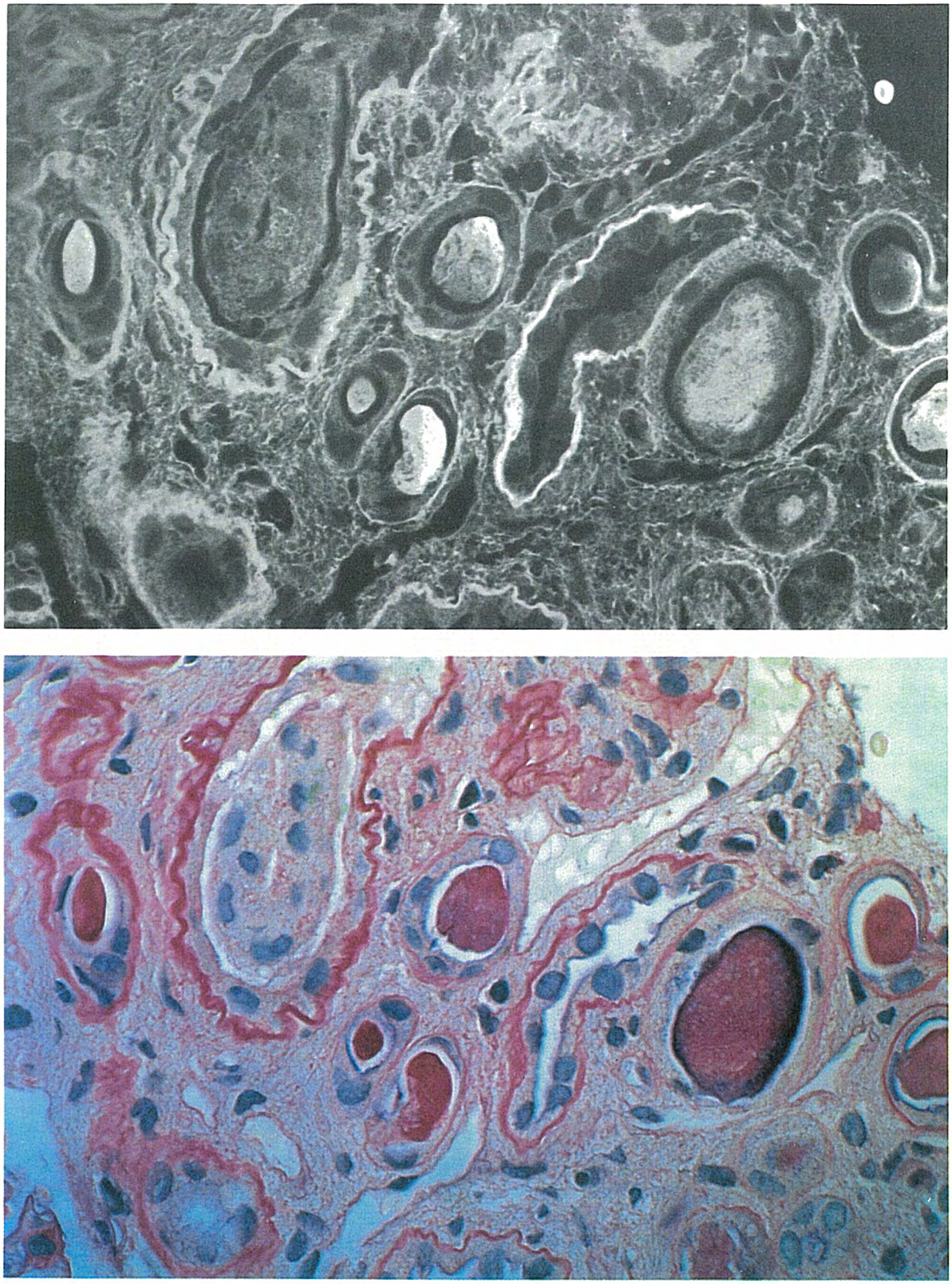

Confocal epifluorescence image (above) with its three-color scanned transmission counterpart (below) of a stained section of diseased human kidney. In both images the height of the field is 144 microns. The confocal image shows fuchsin fluorescence following the PAS technique. The real-color transmission image shows staining by Alcian Blue together with strong purple fuchsin staining in the protein-filled lumen of atrophic tubules. The images were obtained with a Bio-Rad MRC 1000 Confocal System equipped with an argon/krypton laser and the new Bio-Rad three-color transmission detector assembly. This figure illustrates how the absorption image familiar to the pathologist can be formed, with full panning and zooming capability, and readily switched to confocal modes. Image kindly provided by Dr. Sathia Thiru, Department of Medicine, University of Cambridge, U.K. For a more complete discussion of the Bio-Rad MRC 1000, see page 584 in Appendix 2.

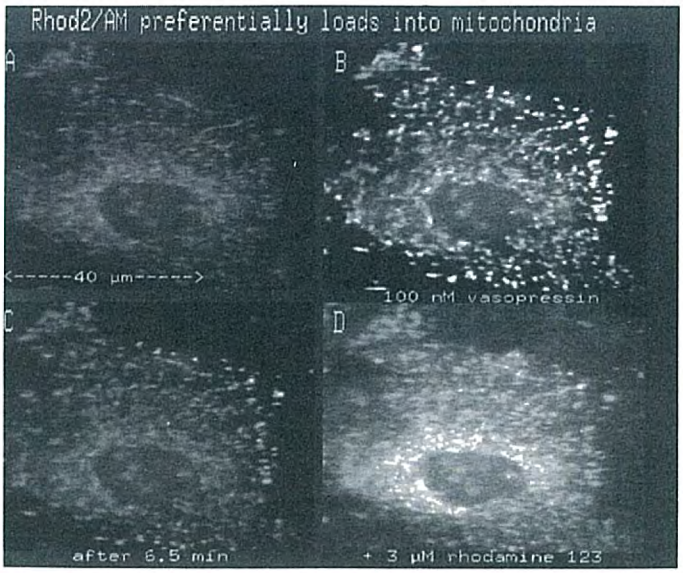

FIGURE 11. Monitoring intramitochondrial [Ca^{2+}] in fibroblasts with rhod-2. Incubation of cells with the acetoxymethyl ester form of rhod-2 (rhod-2/AM) preferentially loads mitochondria with the calcium-sensitive free acid of rhod-2. (A) REF-52 fibroblasts were loaded with 1 µM rhod-2/AM for 1 hr at room temperature and viewed on the UCSD confocal microscope using a green He/Ne laser at 543.5 nm for excitation and a 560-nm long-pass barrier filter for emission. The fluorescence image shows punctate localization of the dye, in contrast to diffuse cytoplasmic fluorescence. (B) 100 nM vasopressin, which elicits a PLC-dependent calcium transient in these cells, also stimulates an intra-mitochondrial [Ca^{2+}] transient, which returns to baseline (C). Subsequent addition of 3 µM rhodamine 123 (D), a selective fluorescent marker for mitochondria, co-localizes with the rhod-2 signal, indicating that the punctate fluorescence from the latter comes preferentially from the mitochondria.

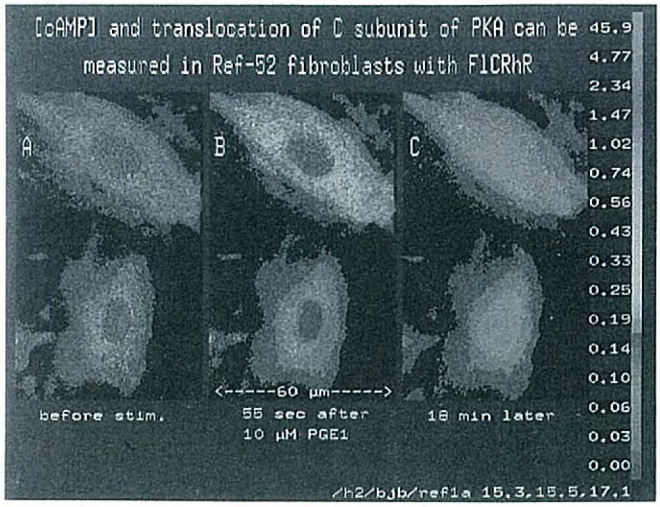

FIGURE 12. Imaging of [cAMP] and of subunits of labeled PKA in single cells. REF-52 fibroblasts were pressure injected with $FlCRhR^{II}$ and imaged on the UCSD confocal microscope using the 488-nm line of an argon laser for excitation. Dual λ fluorescence emission images were recorded simultaneously using barrier filters for fluorescein (510–545 nm) and rhodamine (560 nm long pass). The ratio of the fluorescein image to the rhodamine image was calculated and displayed as pseudocolors on line. (See color insert facing page 472 for color version.) The scale bar to the right represents concentration of cAMP in micromolar, with blues corresponding to low and reds corresponding to high [cAMP], respectively. (A) The two cells exhibit low resting values of [cAMP], and their nuclei are relatively devoid of fluorescence. (B) The cells were stimulated with 10 µM PGE_1, which raised [cAMP] to high levels within 1 min, while the nuclei remained relatively free of fluorescence at this early time. (C) After 18 min, [cAMP] in both cells is still at saturating levels (greater than several micromolar), and the C subunit has had enough time to enter the nuclei, which are no longer dark.

Probably the most important internal messenger aside from Ca^{2+} is cyclic adenosine 3′,5′-monophosphate, or cAMP. Recently it has become possible to image free cAMP concentrations in living cells by use of cAMP-dependent protein kinase labeled with fluorescein and rhodamine on its catalytic and regulatory subunits, respectively (Adams *et al.*, 1991, 1993; Sammak *et al.*, 1992; Bacskai *et al.*, 1993; Tsien *et al.*, 1993). cAMP dissociates the subunits, disrupts fluorescence resonance energy transfer between the attached fluorescein and rhodamine and increases the ratio of fluorescein to rhodamine emissions that result from fluorescein excitation. By contrast, excitation ratioing is much less sensitive to cAMP. A confocal microscope that ratios two emission λs is ideal for imaging the labeled kinase because it ensures accurate registration of the two images and its optical sectioning helps quantify the entry of the free catalytic subunit into the nucleus (Bacskai *et al.*, 1993; Tsien *et al.*, 1993). Figure 12 shows the response to cAMP of the labeled kinase microinjected into fibroblasts. Before stimulation (Fig. 12A), the low ratio of fluorescein to rhodamine emissions indicates that cAMP is very low, as coded by the blue pseudocolors. The nucleus is relatively dark because it excludes the kinase holoenzyme. Soon after addition of prostaglandin E_1, cAMP rises to near-saturating values corresponding to red hues (Fig. 12B), which are well sustained in this cell type and cause gradual translocation of the catalytic subunit into the nucleus (Fig. 12C).

Fixed Specimens

The above emphasis on confocal imaging of live cells might cause concern that video-rate instruments sacrifice the ability to acquire a high-quality through-focus series of images on fixed tissue, the characteristic application for slow-scan confocal microscopes. To allay such concerns, Fig. 13 shows a stereo 3D reconstruction of a thick section of chicken cerebellum in which the Purkinje neurons have been stained by fluorescein-labeled antibodies against the Ca^{2+} storage protein calsequestrin, which localizes within the endoplasmic reticulum of the cell body and dendrites. One-hundred images (each taking no more than 1 sec to acquire) were collected at 0.3-µm intervals along the *z*-axis. Surface contouring and rendering were performed off-line.

A COMMERCIAL AOD-BASED CONFOCAL MICROSCOPE FOR VIDEO AND HIGHER RATES: NORAN INSTRUMENTS ODYSSEY

In 1991, NORAN Instruments (Middleton WI) introduced Odyssey, a video-rate laser-scanning confocal microscope. The Odyssey confocal microscope is based on a design (Draaijer and Houpt 1988) that combines an acousto-optical deflector (AOD) and

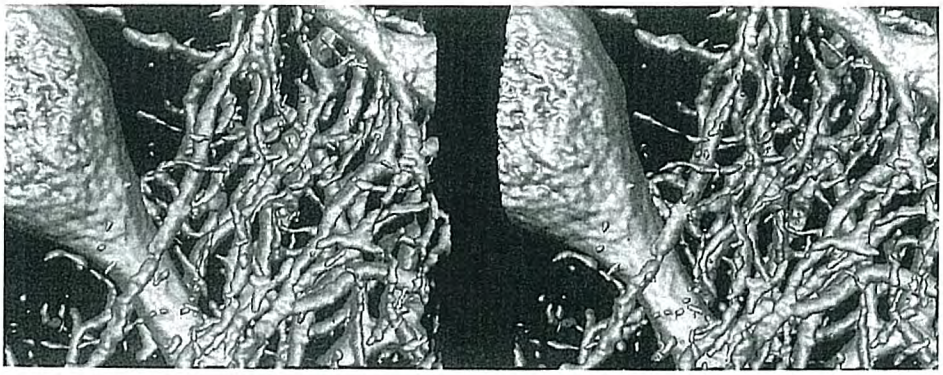

FIGURE 13. Cerebellar Purkinje neurons immunostained for calsequestrin and rendered in 3D. Chicken cerebellum was fixed and stained with a primary antibody against calsequestrin and a fluorescein-conjugated secondary antibody. Calsequestrin is abundant in the endoplasmic reticulum of the Purkinje cell bodies and dendrites but is absent from the spines; 100 serial optical sections were acquired on a Nikon pre-production prototype confocal microscope at 0.3-μm spacing along the *z*-axis. Images were surface-rendered by the "SYNU" program and converted into the stereo-pair displayed here. The dimensions of the volume are 143 μm horizontal × 123 μm vertical × 30 μm deep. We thank Tom Deerinck and Maryann Martone for the specimen and Mark Ellisman and Steve Lamont (all of the San Diego Microscopy and Imaging Resource) for the surface-rendering and stereo display.

a galvanometer-driven mirror to achieve a standard RS-170 video signal output. The Odyssey's video scan generator completes an *x-y* laser scan every 33.33 msec (30 Hz) at 512 horizontal by 480 vertical pixel resolution. Individual pixels are illuminated for 100 nsec during each *xy* scan. During vertical retrace, the laser beam is blanked to minimize sample exposure. Horizontal line scans are accomplished with the AOD, which is a solid-state device with no moving parts. It consists of a glass substrate with an array of piezoelectric transducers bonded to one end. The glass permits operation down to a λ of 351 nm. These transducers are driven at an RF frequency that linearly sweeps from 100 MHz to 200 MHz. The resulting acoustic wave creates a diffraction grating that deflects the incident laser beam. As the RF frequency is swept, so to is the angle at which the diffracted beam exits the AOD. Vertical scan control is achieved by guiding the diffracted beam to a galvanometer mirror oscillating at a 60 Hz rate.

Since the sweep rate of RF frequencies can be controlled, the AOD can be used to produce variable horizontal scan rates. A 15.625-kHz horizontal scan rate is required for RS-170 timing specification. However, the AOD scan may be stopped entirely so that a diffraction-limited spot (an Airy disk) illuminates the sample. This spot may be panned to any position within the scanned field of view area.

The diffraction efficiency of the AOD can be controlled by varying the RF power input to the AOD. This is a convenient way to control the laser intensity incident to the sample and implement fast shuttering. In addition, since the sweep rate and range of acoustic frequencies input to the AOD can be controlled electronically, the AOD effectively provides continuous image pan and zoom. The optical diagram (Fig. 14) shows a view of the optical bench layout as seen with the main panel of the Odyssey scan module removed. The laser is mounted on the back of the main base plate, and the beam is directed by a mirror through a small hole in the base plate. Immediately above the hole is a filter wheel. One filter at a time may be moved in front of the beam as directed by the host computer. After the filters, the beam reflects off a polarizing beamsplitter and then passes through a beam expander and beam shaping optics in order to fill the aperture of the AOD.

After the AOD, the beam is reshaped back to a circular profile and collimated by a small set of lenses and then reflected off the primary dichroic mirror. Motorized control of the doublet after the AOD is used to correct any astigmatism introduced by the AOD when changing either the laser illumination λ or the zoom factor.

Odyssey dichroics are custom-made with high-efficiency coatings and are mounted in Nikon-style cubes. The Odyssey has fluorescence, reflective and transmitted light detection channels, which can be used in combination for different applications. Fluorescence and reflective channels use high-efficiency side-on PMTs. However, images generated by the transmitted light detector is non-confocal. Following the galvanometer mirror, the beam is directed down a relay tube and into the optical microscope through its camera port. A focusing lens and a field lens are designed to match the beam to both the image plane and the pupil plane of the microscope. Because the pupil position varies for different microscopes, these lenses are selected specifically for each type of microscope.

Because the AOD has limited diffraction efficiency and is λ dependent, it cannot be used to descan the emitted fluorescence from a sample. In the Odyssey, a separate light path has been added to capture emitted fluorescence after its vertical excursion has been descanned by the galvanometer. Because the fluorescence beam has not been horizontally descanned, it is still oscillating linearly and is projected onto a slit rather than a pinhole in front of the fluorescence detectors. This combination of point illumination with slit detection of fluorescence constitutes an intermediate case between point- and line-scanning confocal systems, as discussed in Chapters 21 and 25. Slits of six different widths from 10–250 μm are printed on the slit plate and are selected by motorized linear translation of that plate. A secondary dichroic mirror then permits detection of fluorescence by two PMTs monitoring separate emission bands.

The AOD can be used to descan reflected light, permitting fully confocal operation in this mode. Although the lenses in the Odyssey are antireflection coated, some back reflections off the lenses still occur. To reduce their contribution, a quarter-wave

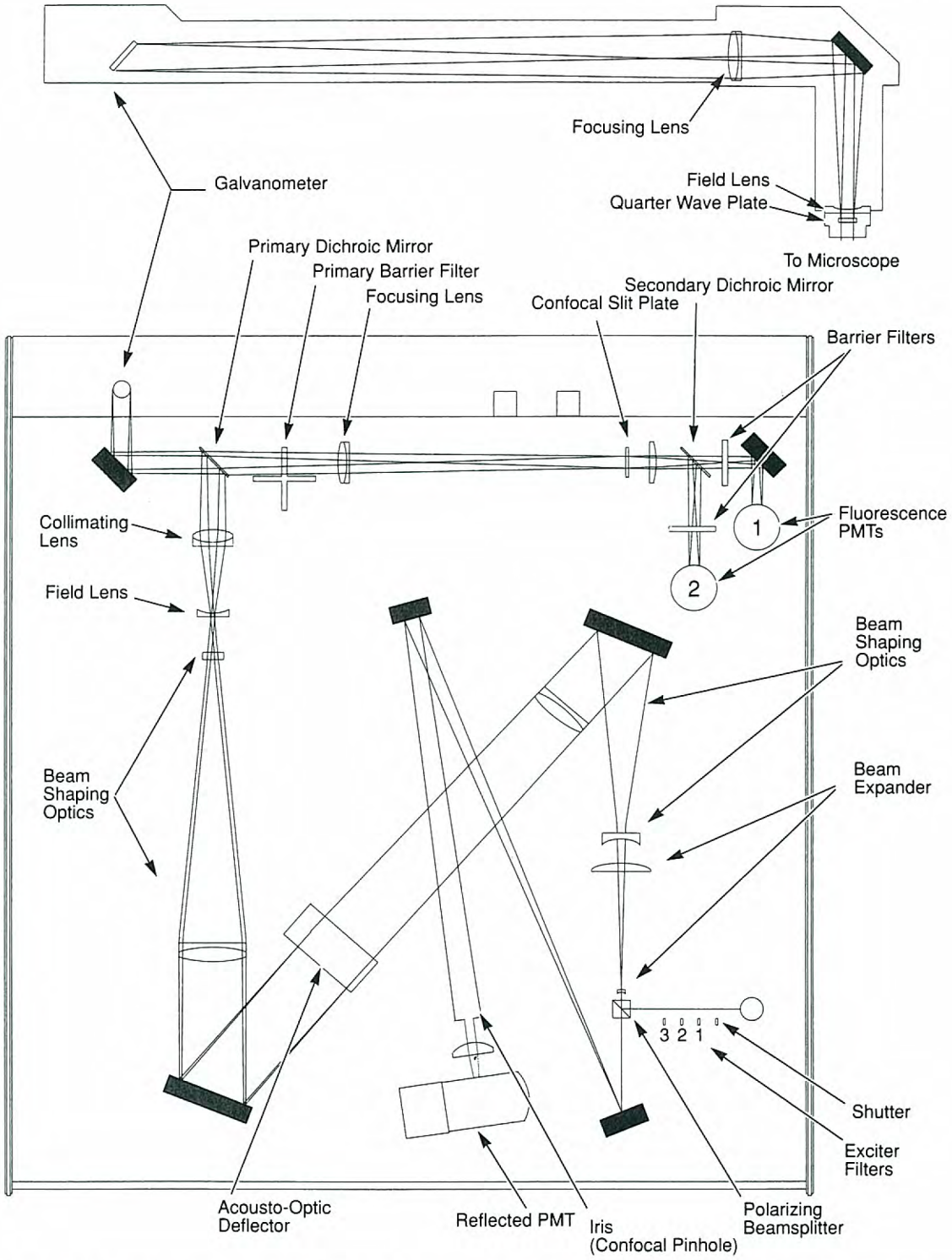

FIGURE 14. Optical layout of Noran Instruments Odyssey confocal microscope system. Cutaway view showing the excitation and collection paths. A multiline argon or krypton–argon ion laser is attached to the back side of a heavy optical baseplate. Linearly polarized laser light enters through a hole in the baseplate and passes through a narrow-bandpass filter to select one laser line. The excitation light travels through an AOD (providing the x-scan), reflects off a galvanometer mirror (providing the y-scan) and travels down a relay tube into the camera port of a standard optical microscope. Light emitted by the sample travels back down the relay tube to the primary dichroic mirror. Fluorescent light passes through the primary dichroic and down a separate detection path with a confocal slit aperture to the PMT. Reflected light travels back through the AOD and polarizing beamsplitter and finally through a confocal pinhole. The polarizing beamsplitter and quarter-wave plate serve to reject unwanted reflections off the optical components.

retardation plate is installed at the end of the relay tube or in some cases in the microscope itself. The polarizing beamsplitter reflects light polarized perpendicular to the plane of the main optical diagram (*s*-polarization) and transmits light polarized parallel to the page (*p*-polarization). Light reflected from optical elements between the polarizing beamsplitter and the quarter-wave retarder still has *s*-polarization, so the polarizing beamsplitter dumps it by reflecting it into the laser. Reflections originating after the quarter-wave retarder up to and including the specimen traverse the quarter-wave plate twice, becoming *p*-polarized. This rotation permits such reflected light to be transmitted through the polarizing beamsplitter. It then passes through an adjustable, automated iris diaphragm, which has sufficient range to achieve confocal and nonconfocal observations, and is detected by a side-on PMT.

In the original Odyssey, the analog signal generated by the PMTs was fed immediately to an output stage where it was translated into a RS-170-compatible video signal for direct viewing on a monitor or processing by a frame grabber in a separate host computer. In late 1993, NORAN introduced a new version called the Odyssey XL, which added variable rate scan control features and fast digital image processing hardware. While the Odyssey XL is based on the same optical layout used in the Odyssey, the XL's new Dynamic Scan Control hardware was added to provide greater control over the Odyssey's point scanning mechanism as well as to incorporate important video-rate image processing features like background subtraction and averaging. Image scan rates, resolution and pixel dwell-time can be controlled to tailor the Odyssey XL's image capture and preprocessing facilities for later acquisition and analysis on the host computer. Table 3 shows the variable scan options available with the Odyssey XL. The pixel dwell-time, defined as the period of time during which excitation and detection occur for each pixel, can vary from 100 nsec up to 6.4 μsec, whereas the original Odyssey had a fixed pixel dwell-time of 100 nsec. Analog-to-digital converter (ADC) sample rates are adjusted according to the pixel dwell-time. For slower dwell-times (>800 nsec) the PMT signal is directed to an integrator stage prior to the ADC to accumulate over entire dwell-times. The Odyssey XL is the first laser confocal system in which scan frequencies from below to above normal video rate (Table 3) are supported.

Table 3. Variable Scan Options for the Noran Odyssey XL

Image size	Frame rate (Hz)	Scan time per image	Pixel dwell-time (nsec)
128 × 120	240	4.6 msec	100
256 × 240	120	8.3 msec	100
256 × 240	30	33.3 msec	400
512 × 480	30	33.3 msec	100
512 × 480	15	66.7 msec	200
512 × 480	7.5	133.3 msec	499
512 × 480	3.7	266.7 msec	800
512 × 480	1.8	533.3 msec	1,600
512 × 480	1	1067.0 msec	3,200
1024 × 960	1.8	0.5 sec	400
1024 × 960	1	1.0 sec	800
1024 × 960	0.5	2.1 sec	1,600
1024 × 960	0.2	4.3 sec	3,200

Only one ADC is presently in the system, so that when two detection channels are being used, the ADC alternates between those channels line-by-line. This multiplexing avoids having to double the output bandwidth but discards one-half the photons because each channel is being observed only every other line. The vertical resolution for each individual channel is also halved, and the two images are out of vertical register by the width of 1 line.

The Odyssey XL video output stage includes both a CCIR 601-compatible digital video output and a RS-170 analog video output. The Dynamic Scan Control hardware embeds control information into each video frame that describes key scanning parameters and data organization. Acquisition software executed on the host computer interprets this control information and then, as a result, decides how to process, display, and store the acquired data. If two detection channels are in use, such processing includes demultiplexing the two interleaved images.

The digital video output enables the Odyssey XL to transfer the digital image data directly to a host computer, bypassing conversion to an analog video stream and subsequent conversion back again to digital image data in the host computer. This avoids quantization errors that occur in both the digital-to-analog conversion within the Odyssey (analog video output stage) and also the analog-to-digital conversion done by the framegrabber in the host computer. The NORAN InterVision imaging system can acquire either digital or analog video data streams from the Odyssey XL.

The Dynamic Scan Control hardware is based on a dual TMS34020 graphics processor (GSP) architecture, which also includes a separate, fast arithmetic logic unit (ALU). Acquisition memory is 1024 × 512 × 16 bits deep and is used to store data digitized by a 10 MHz 8-bit ADC. Full 1024 point line scans can be stored in the acquisition memory. The ALU can do background subtraction, accumulation (summing) and averaging operations on data in the acquisition memory at video rate. Results from an ALU operation are stored in display memory for eventual output in either digital or analog video formats. Ratioing of two emission channels would have to be done in the host workstation after de-multiplexing the two channels; ratioing is not yet supported but is among the functions being considered for software implementation.

The display memory is controlled by a dedicated TMS34020 GSP, which enables the Dynamic Scan Control hardware to decouple acquisition timing requirements from display and RS-170 video synchronization requirements. Thus even if the Odyssey XL is scanning at the slowest possible rate, it still maintains an RS-170-compatible video output. When scanning at frame rates higher than 30 Hz, the individual images, each of reduced size, are displayed as subtiles of a normal 512 × 480 image updated at 30 Hz, so that they can be viewed by normal display monitors. When two channels are undergoing multiplexed acquisition, they are respectively displayed as interlaced fields of the composite frame.

Reference (e.g., background) images can be captured and stored locally for subsequent ALU operations. Like acquisition memory, data stored in the background memory can be transferred to the display memory for output. This makes it possible for the Odyssey XL operator to switch between different displayed (output) images interactively.

Currently, image sequences obtained at high speed can only be stored in the main memory of the host workstation. When this

is filled, recording must stop while the data are transferred to the workstation hard disk. Future plans include use of a video compression board in the workstation. Such compression (using the lossy JPEG standard) should eventually permit continuous storage to hard disk at 30 frames/sec. No interface with video optical memory disk recorders (OMDRs) is planned.

CONCLUSIONS AND PROSPECTS FOR THE FUTURE

At first glance, video-rate scanning might seem just to offer a speed advantage over conventional confocal microscopy. But real-time confocal microscopy gives the user a qualitatively different feel from slow-scan instrumentation, much as a camcorder has a different feel from a still camera even if the latter has a motorized film advance. Continuous sequences of moving cells or dynamic biochemistry can be recorded and analyzed as well as static individual frames. However, such performance requires not only rapid scanning but also the ability to store, catalog, ratio and retrieve hundreds or thousands of frames from one or two channels acquired at 30 or 15 frames/sec. It would be wasteful to couple a video-rate scanner to an underpowered image processor, software package and storage system that cannot cope with the resulting data stream.

What are the disadvantages of video-rate scanning? For the true-confocal system commercially available from Nikon, high cost is perhaps the most obvious. The resonant scanner itself is not expensive, but the electronics that compensate for the sinusoidal scan do add some complexity and cost, to which must be added the high-speed image processor, optical memory disk recorder and complex real-time software, which would be required in any serious system for fast recording. All the current video-rate systems—UCSD, Nikon, and Noran—have 512 horizontal × ~484 vertical pixels, whereas many slower laser-scanning systems have higher numbers of pixels. Optical zooming is relatively difficult on a resonant scanner since not only the scanner amplitude but also the magnification of the registration grating with respect to the specimen must be altered. Finally, the nonuniform scan velocity may cause subtle differences between the center and the edges of an image with respect to lateral resolution, bleach rate, and susceptibility to output saturation due to ground-state depletion. We ourselves have not found such lateral nonuniformities to be a significant problem, given that optical systems already generally perform better on-axis compared to off-axis, but our experience has been mostly with diffusible fluorescent indicators. Differential bleaching might be more noticeable with fixed specimens.

For AOD-based confocal microscopes, such as the Noran Odyssey, the main disadvantage seems to be the slit confocality in fluorescence mode, giving a linear instead of a quadratic intensity fall-off in depth as in pinhole confocal systems. However, this will only be noticeable for thick specimens with many fluorescing features. The dispersiveness of the AOD is the source of effects such as image shifts when changing λs, but with proper software this can be handled without problems.

What about scanning faster than 30 frames/sec? The advent of high-definition television (HDTV) should make higher-resolution video much cheaper to display and store. Even with current video standards, rates up to 120–240/sec would not be difficult and could be useful for imaging cytosolic Ca^{2+} in excitable cells. Such image rates would be most easily achieved by sacrificing resolution or field of view. The Noran Odyssey XL already implements high-speed imaging in this way; fairly similar modifications made to trade numbers of pixels for frame rate should be possible for resonant galvanometer scanning. The ultimate in speed would be achieved with the *y*-axis scan disabled altogether, resulting in line scanning at 15.75 kHz. The *y*-axis of the display would represent time at 63.5 μsec/line, rather than any spatial extent. Are there any biological phenomena requiring such speed? Action potentials, synaptic events, and localized Ca^{2+} changes near the mouths of Ca^{2+} channels occur at millisecond or faster time scales. However, confocal imaging of such signals would probably require major improvements in voltage- and Ca^{2+}-sensitive dyes, not just faster instrumentation. Existing voltage-sensitive dyes are fast enough but give miniscule changes in fluorescence for physiological voltage changes, whereas present Ca^{2+}-sensitive fluorescent indicators probably have too-high affinities and slow kinetics and may lack the spatial resolution to see submicroscopic local domains of high Ca^{2+} concentrations. Improvement in indicator molecules may become the limiting factor because their development does not enjoy the commercial rewards that motivate the intensive competition in computers and video processing.

SUMMARY

Laser confocal point scanning at video rate (15,750 lines/sec) can be achieved without the traditional compromises of slit excitation, slit detection or a reduced number of pixels. A resonant galvanometer is an optically simple and efficient scanner, whose only drawback is that it generates sinusoidal rather than sawtooth motion. However, this problem is readily overcome by electronics that reformat the stream of pixel data. Practical instruments exciting with UV or visible λs and collecting single or dual emission λs with instantaneous ratioing are now commercially available and are particularly valuable for studying high-speed signaling in living cells. Dynamic ratio images of Ca^{2+} (obtained at 15–30 Hz) and cAMP are demonstrated. Instruments using AODs to provide the high-speed scan for video-rate imaging are also now available. They have a higher duty cycle and can be fitted with hardware Zoom magnification with greater ease, but they are limited to using a slit confocal aperture when operated in the fluorescent mode.

ACKNOWLEDGMENTS

The original funding for the UCSD prototype video-rate confocal microscope was from the National Science Foundation, grant BBS-8714246. Subsequent support came from NIH grant NS27177 and the Howard Hughes Medical Institute. We also thank the biological collaborators listed in the individual figure legends, as well as the Nikon Corp. and Nikon Inc. confocal microscope teams, especially R. Chu, J. Dow, Y. Itoh, K. Ogino, K. Onogi, H. Ooki, S. Schwartz, T. Shiihashi, and M. Yamasaki, for technical information and assistance in preparing Table 2 and Figs. 6, 7, 8, 9, and 12. The description of acousto-optical deflection systems

was heavily revised by A. Draaijer, B. Batten, and J. Lalonde, who also contributed the description of the Noran Odyssey systems, Table 3, and Fig. 14. Finally, we thank Anastasia Clark for preparation of Figs 1–5 and expert editorial assistance.

REFERENCES

Adams, S.R., Harootunian, A.T., Buechler, Y.J., Taylor, S.S., and Tsien, R.Y., 1991, Fluorescence ratio imaging of cyclic AMP in single cells. *Nature* 349:694–697.

Adams, S.R., Bacskai, B.J., Taylor, S.S., and Tsien, R.Y., 1993, Optical probes for cyclic AMP. In: *Fluorescent Probes for Biological Activity of Living Cells—A Practical Guide* (W.T. Mason, ed.), Academic Press, San Diego, pp. 133–149.

Art, J.J., and Goodman, M.B., 1993, Rapid scanning confocal microscopy. In: *Cell Biological Applications of Confocal Microscopy: Methods in Cell Biology* (B. Matsumoto, ed.), Academic Press, San Diego, San Diego, pp. 44–77.

Bacskai, B.J., Hochner, B., Mahaut-Smith, M., Adams, S.R., Kaang, B.-K., Kandel, E.R., and Tsien, R.Y., 1993, Spatially resolved dynamics of cAMP and protein kinase A subunits in *Aplysia* sensory neurons, *Science* 260:222–226.

Cohen-Sabban, J., Rodier, J.C., Roussel, A., and Simon, J., 1984, Ophthalmoscope—A balayage optique. *J. Optics (Paris)* 15:425–430.

Denk, W., Strickler, J.H., and Webb, W.W., 1990, Two-photon laser scanning fluorescence microscopy, *Science* 248:73–76.

Dickson, L.D., and Sincerbox, G.T., 1991, Holographic scanners for bar code readers. In: *Optical Scanning* (G.F. Marshall, ed.), Marcel Dekker, New York, pp. 159–212.

Draaijer, A., and Houpt, P.M., 1988, A standard video-rate confocal laser-scanning reflected and fluorescence microscope, *Scanning* 10:139–145.

Draaijer, A., and Houpt, P.M., 1993, High scan-rate confocal laser scanning microscopy. In: *Electronic Light Microscopy: Techniques in Modern Biomedical Microscopy* (D. Shotton, ed.), Wiley–Liss, New York, pp. 273–287.

Froome, K.D., and Essen, L., 1969, *The Velocity of Light and Radio Waves*, Academic Press.

Gan, X.S., and Sheppard, C.J.R., 1993, Detectability: A new criterion for evaluation of the confocal microscope, *Scanning* 15:187–192.

Goldstein, S.R., Hubin, T., Rosenthal, S., and Washburn, C., 1990, A confocal video-rate laser-beam scaning reflected-light microscope with no moving parts, *J. Microsc.* 157:29–38.

Goldstein, S.R., Hubin, T., and Smith, T.G., Jr., 1992, An improved no-moving-parts video-rate confocal microscope, *Micron Microsc. Acta* 23:437–446.

Gottlieb, M., 1991, Acoustooptic scanners and modulators. In: *Optical Scanning* (G.F. Marshall, ed.), Marcel Dekker, New York, pp. 615–686.

Kramer, C.J., 1991, Holographic deflector for graphic arts systems. In: *Optical Scanning* (G.F. Marshall, ed.), Marcel Dekker, New York, pp. 213–350.

Marshall, G.F. (ed.), 1991, *Optical Scanning*, Marcel Dekker, New York.

Minta, A., Kao, J.P.Y., and Tsien, R.Y., 1989, Fluorescent indicators for cytosolic calcium based on rhodamine and fluorescein chromophores, *J. Biol. Chem.* 264:8171–8178.

Montagu, J.I., 1991, Galvanometric and resonant low-inertia scanners. In: *Optical Scanning* (G.F. Marshall, ed.), Marcel Dekker, New York, pp. 525–613.

Niggli, E., and Lederer, W.J., 1990, Real-time confocal microscopy and calcium measurements in heart muscle cells: Towards the development of a fluorescence microscope with high temporal and spatial resolution, *Cell Calcium* 11:121–130.

Rizzuto, R., Simpson, A.W.M., Brini, M., and Pozzan, T., 1992, Rapid changes of mitochondrial Ca^{2+} revealed by specifically targeted recombinant aequorin, *Nature* 358:325–327.

Round, F.E., Crawford, R.M., and Mann, D.G., 1990, *The Diatoms: Biology and Morphology of the Genera*, Cambridge University Press, New York.

Sammak, P.J., Adams, S.R., Harootunian, A.T., Schliwa, M., and Tsien, R.Y., 1992, Intracellular cyclic AMP not Ca^{2+} determines the direction of vesicle movement in melanophores: Direct measurements by fluorescence ratio imaging, *J. Cell Biol.* 117:57–72.

Shepherd, J., 1991a, Bearings for rotary scanners. In: *Optical Scanning* (G.F. Marshall, ed.), Marcel Dekker, New York, pp. 477–524.

Shepherd, J., 1991b, Windage of rotating polygons. In: *Optical Scanning* (G.F. Marshall, ed.), Marcel Dekker, New York, pp. 451–476.

Sherman, R.J., 1991, Polygonal scanners: Applications, performance, and design. In: *Optical Scanning* (G.F. Marshall, ed.), Marcel Dekker, New York, pp. 351–408.

Sims, P.A., 1983, A taxonomic study of the genus *Epithemia* with special reference to the type species *E. turgida* (Ehrenb.) Kütz, *Bacillaria* 6:211–235.

Takamatsu, T., and Wier, W.G., 1990, High temporal resolution video imaging of intracellular calcium, *Cell Calcium* 11:111–120.

Taylor, W.H., 1984, Characteristics of a new compact video rate optical scanner (CVROS), *SPIE* 518:7–14.

Toyen, G., 1976, Generation of precision pixel clock in laser printers and scanners, *SPIE* 84:138–145.

Tsien, R.Y., Bacskai, B.J., and Adams, S.R., 1993, FRET for studying intracellular signalling, *Trends Cell Biol.* 3:242–245.

Tsien, R.Y., and Harootunian, A.T., 1990, Practical design criteria for a dynamic ratio imaging system, *Cell Calcium* 11:93–109.

Webb, R.H., Hughes, G.W., and Pomerantzeff, O., 1980, Flying spot TV ophthalmoscope, *Appl. Optics* 19:2991–2997.

Webb, R.H., 1984, Optics for laser rasters. *Appl. Optics* 23:3680–3683.

Webb, R.H., Hughes, G.W., and Delori, F.C., 1987, Confocal scanning laser ophthalmoscope, *Appl. Optics* 26:1492–1499.

White, J.G., Amos, W.B., and Fordham, M., 1987, An evaluation of confocal versus conventional imaging of biological structures by fluorescence light microscopy, *J. Cell Biol.* 105:41–48.